drones

*Article*

# The Potential of UAV-Acquired Photogrammetric and LiDAR-Point Clouds for Obtaining Rock Dimensions as Input Parameters for Modeling Rockfall Runout Zones

**Barbara Žabota [1,2], Frédéric Berger [3] and Milan Kobal [2,*]**

[1] Flycom Technologies d.o.o., Ljubljanska cesta 24a, 4000 Kranj, Slovenia
[2] Department of Forestry and Forest Renewable Resources, Biotechnical Faculty, University of Ljubljana, Večna pot 83, 1000 Ljubljana, Slovenia
[3] Unité de Recherche Érosion Torrentielle, Neige et Avalanches (INRAE, UR ETNA), French National Research Institute for Agriculture, Food and the Environment, 38402 St-Martin-d'Hères, France
* Correspondence: milan.kobal@bf.uni-lj.si; Tel.: +386-1-3203529

**Abstract:** Rockfalls present a significant hazard to human activities; therefore, their identification and knowledge about potential spatial impacts are important in planning protection measures to reduce rockfall risk. Remote sensing with unmanned aerial vehicles (UAVs) has allowed for the accurate observation of slopes that are susceptible to rockfall activity via various methods and sensors with which it is possible to digitally collect information about the rockfall activity and spatial distributions. In this work, a three-dimensional (3D) reconstruction of rock deposits (width, length, and height) and their volumes are addressed, and the results are used in a rockfall trajectory simulation. Due to the availability of different sensors on the UAV, the aim was also to observe the possible differences in the dimension estimations between photogrammetric and LiDAR (light detection and ranging) point clouds, besides the most traditional method where rock deposit dimensions are measured on the field using a measuring tape. The motivation for reconstructing rock dimensions and volumes was solely for obtaining input parameters into a rockfall model. In order to study the differences between rock-measuring methods, rock dimensions were used as input parameters in a rockfall model, and additionally, modeling results such as propagation probability, maximum kinetic energies, and maximum passing heights were compared. The results show that there are no statistically significant differences between the measurement method with respect to rock dimensions and volumes and when modeling the propagation probability and maximum passing heights. On the other hand, large differences are present with maximum kinetic energies where LiDAR point cloud measurements achieved statistically significantly different results from the other two measurements. With this approach, an automated collection and measurement process of rock deposits is possible without the need for exposure to a risk of rockfall during fieldwork.

**Keywords:** rockfall; UAV; LiDAR; photogrammetry; modeling; input parameters



**Citation:** Žabota, B.; Berger, F.; Kobal, M. The Potential of UAV-Acquired Photogrammetric and LiDAR-Point Clouds for Obtaining Rock Dimensions as Input Parameters for Modeling Rockfall Runout Zones. *Drones* **2023**, *7*, 104. https://doi.org/10.3390/drones7020104

Academic Editor: Giordano Teza

Received: 23 December 2022
Revised: 26 January 2023
Accepted: 31 January 2023
Published: 3 February 2023



## 1. Introduction

Rockfalls are a widespread phenomenon, especially in mountain areas. They are unpredictable and extremely rapid processes [1,2] that exhibit high kinetic energies, and thus, have large damage capacities, often resulting in human casualties and damage inflicted on infrastructure [3,4]. Rockfalls occur when a fragment of a rock or block detaches from a steep slope or cliff [5], and the moving mass travels mostly through the air by free fall, leaping, bounding, or rolling, with little or no interaction with other moving rocks [6]. The combination of different factors influences the detachment of the rocks, including geological predispositions, climate conditions (e.g., freeze–thaw cycle), weather (intensive rain periods), seismic activity, vegetation growth, etc. [7]. The fragmentation of rocks down the slope provides information for reconstructing trajectories and for further performing

run-out analyses. In the detachment process of the rocks from the rockfall source (e.g., rock wall and steep slope), rocks will be fragmented and reach different volumes and kinetic energies, and due to the impacts, the rocks will be scattered along the slope [8].

In order to implement either technical protection measures (e.g., rockfall dams and flexible nets) or biological measures (e.g., protection forests), an assessment of rockfall hazards and risks is necessary. Assessments of this phenomenon in time and space remain a challenge as they include various factors. These include the location of the rockfall source area, the frequency and volumes of detached rock mass, the fragmentation of the detached rock mass, the size and the shape of the moving rock mass, the dissipation of the kinetic energy during rebounds and impacts with trees or lying logs [9]. Realistic predictions of the rockfall's runout area are possible by modeling rockfall trajectories and the maximum extent of rockfall runout zones with rockfall trajectory simulations [10–13]. The results of such simulations are, e.g., propagation probability, kinetic energies, passing heights of simulated rocks, the number of passing rocks, energy line angles, etc. Modeling results are further used in planning technical protection measures, e.g., for planning the locations of rockfall nets, screens, and barriers; for calculating kinetic energy, vertical passing heights, velocities, rotational velocity, impact angles, and passing heights of rocks when they arrive in nets [10–13]. In quantitative hazard and risk analyses of rockfalls, the quantification of rock deposits and their fragmentation is needed [8]. The distribution of deposited rock masses and their volumes will be key in reconstructing past rockfall trajectories and defining runout zones and the magnitude of rockfall events [13]. If realistic rock sizes will be used in rockfall models, the modeled trajectories and kinetic energies will be more realistic [8].

To calibrate the rockfall models accordingly to real past situations, key data will be the locations and dimensions of corresponding deposited rock masses [14], as the dimensions and volumes of the rocks are input parameters for rockfall models. This will require the use of existing inventories about past events; however, these inventories might vary and can be based on different sources, and they might not always contain quantitative and detailed information (e.g., dimensions or volumes) about the rock masses [15–18]. The issue with existing rockfall databases is that they often have low spatial accuracy, poor information about the rockfall event, and lack information on the rock masses' dimensions or volumes [14], which are usually only recorded at the maximum runout areas. Therefore, field collection is required to obtain truthful and reliable data on past events [8,14]. However, field collection can be challenging [19], mainly because rockfalls occur in mountainous areas that are remote and difficult to access. The collection of data, e.g., the dimensions of deposited rock masses, is labor-intensive and time-consuming since measurements are performed by hand using a measuring tape and are dangerous since new rockfall events during field collection operations might occur again [8,14,20,21].

Methodologies that propose an objective and systematic collection of rockfall deposits and their dimensions are limited. Ruiz-Carulla et al. [21] presented a methodology for mid-size fragmented rockfalls ($10^3$ up to $10^5$ $m^3$) that consists of counting and measuring block fragments in selected sampling plots with homogeneous zones in young debris covers as well as large and scattered rocks. Biagi et al. [18] proposed a three-step procedure for the collection of rock deposits at the foot of a slope, combining data from the existing catalogue of events and measured volumes that have fallen down the slope. Žabota and Kobal [14] showed a method comprising the collection of the representative spatial distribution of rock deposits within rockfall runout zones with the use of a mobile application. Marchelli and De Biagi [22] presented a method for collecting rockfall deposits by determining one or more homogeneous area within the rockfall runout, and in each area, a sampling subarea is identified. Furthermore, each subarea is then divided into four equally sized areas where the sampling is performed. Wegner et al. [23], in their approach, measured the rocks deposited on the talus's surface, covering the upper and lower parts of the talus cones. In that study, rocks only had one dimension (width/length/height), measuring at least 0.5 m.

To overcome the limitations of hand-measuring methods on the field and potentially increase the sample of measured rocks, we can currently take advantage of different digital 2D and 3D data. With modern remote sensing techniques, with respect to surveying, such as unmanned aerial vehicles (UAVs) in combination with different sensors (e.g., RGB cameras; light detection and ranging—LiDAR; multispectral or hyperspectral cameras) [24], obtaining high-resolution LiDAR, and photogrammetric products are possible. There has been a substantial expansion with respect to UAV photogrammetry and LiDAR in the application of studying rockfall activities. This technology has the ability to remotely capture exposed and endangered areas, allowing for both safe and efficient work while simultaneously providing high-resolution data (up to a few centimeters) [25,26].

These applications have been observed with the monitoring of rockfall activity; the detection of early movements; the characterization of joints, discontinuities, and detachments in slopes; the reconstruction of detached rock dimensions and volumes; the modeling of rockfall runout zones, and the production of risk and susceptibility maps; and monitoring forests with protective effects against rockfalls, etc. [4,27–37]. The key feature of UAV remote sensing data is the three-dimensional surface (3D point cloud), which is either surveyed with LiDAR sensors or produced with structure from motion (SfM) techniques from images. Digital surface models (DSMs) provide data about the terrain, vegetation, and other features in the landscape that could be subjects in rockfall risk analyses (e.g., infrastructure, buildings, and vegetation [27]). With the classification of 3D point clouds, it is possible to create a digital terrain model (DTM) that represents the main geometrical characteristics of the surface.

Several authors have shown that UAV remote sensing data can effectively be used for reconstructing rockfall activity. Sarro et al. [27] used UAV photogrammetric 3D point clouds to determine the average size and volume of the rocks that are detached from the rock wall. The data were implemented in RockPro3D software, which was used to obtain the travelling distance of the rocks. Spreafico et al. [38] used the results of the UAV photogrammetric survey for the block identification and classification of their surfaces and further compared the rock-scattering results with the results of a discrete fracture network (DFN) model. Vanneschi et al. [7] used UAV photogrammetric 3D point clouds to identify and measure rocks in order to use them in the 3D modeling of rockfall trajectories using Rockyfor3D. Robiati et al. [39] extracted a digital surface model from SfM and Multiview Stereopsis (MVS) and rock sizes to model rockfall runout zones using two models: Rocfall and Rockyfor3D. Francioni et al. [40] used UAV photogrammetric point clouds to extract rock volumes as inputs for rockfall simulations. They digitalized over 600 rocks on orthophotographs with volumes larger than 1 $m^3$ to calibrate rockfall modeling with Rockyfor3D. Gallo et al. [41] derived a digital elevation model from UAV photogrammetry, in combination with photos identified, and they measured more than 600 brocks in the GIS software. The measured rocks were further used in modeling rockfall runout areas with RocPro3D.

To overcome the issues related to the measurement of rock deposits on the field and to obtain a representative sample in order to model rockfall trajectories and potential runout zones, this study aims to gather the required data with UAVs. In particular, different sensors mounted on UAVs can be used for obtaining input parameters for rockfall modeling. The purpose of this study was to obtain the locations of the rockfall deposits and their dimensions (length, width, and height) in order to perform a reconstructive analysis of rockfall events. Within the scope of this paper, a methodology for obtaining a representative sample of rock deposits and their dimensions is presented, while using the measured values in the 3D modeling of rockfall propagation and runout zones. Additionally, in order to reduce the amount of fieldwork and tape measurement of individual rocks, measurements of selected rockfall rock deposits on the field were carried out in order to directly compare them to the measurements of the same rocks using UAV LiDAR and photogrammetric point cloud scanning. The decision made on including different sensors in the study was to provide insights on which sensors are more/less appropriate for collecting data on

rock dimensions and volumes, and the motivation for deciding on the sensor is largely related to their different costs (e.g., RGB cameras mounted on commercial UAVs vs. UAV LiDAR sensors), and abilities with respect to covering different surface areas. The research question is as follows: will there be statistically different or similar results in the modeling of rockfall runout zones when using photogrammetric or LiDAR point cloud as a source of rock dimensions and volume measurements, in comparison to the field measurements? Moreover, the values of the measured rocks based on three methods were further used in modeling the rockfall runout zone to test if the differences between the measurement methods influence the final modeling results. With that purpose, three modeling results were compared between the measuring methods: maximum runout zones, kinetic energies, and the passing heights of rocks were statistically compared.

## 2. Materials and Methods

### *2.1. Study Area*

There were three study sites in this research study, and all are located in the Julian Alps, in the northwestern part of Slovenia (Figures 1 and 2). Krnica and Kekec rockfalls are located within glacial alpine valleys, while the Mangart rockfall is located on a mountain pass.

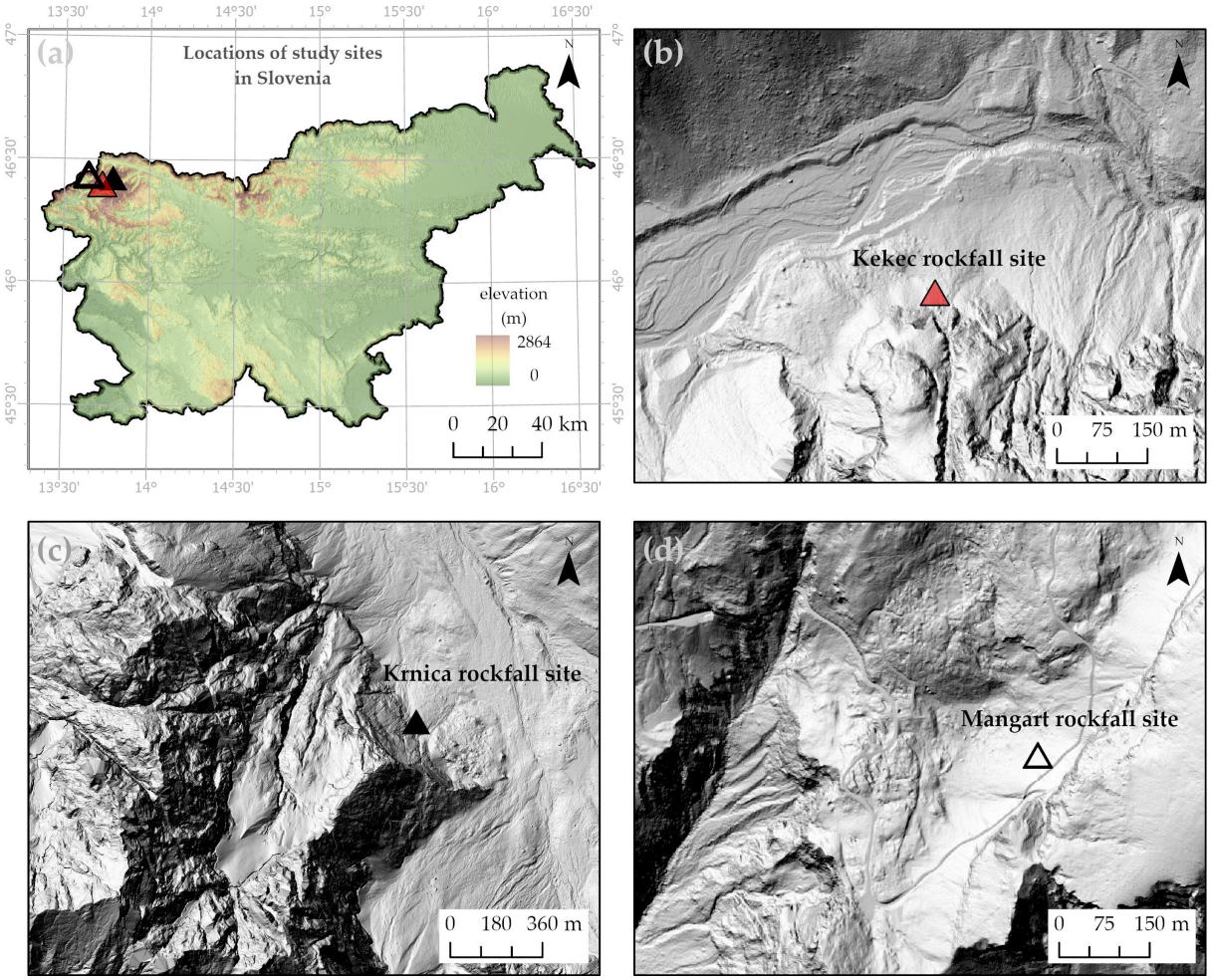


**Figure 1.** (**a**) Locations of rockfall study sites in Slovenia, (**b**) Kekec rockfall site, (**c**) Krnica rockfall site, and (**d**) Mangart rockfall site.

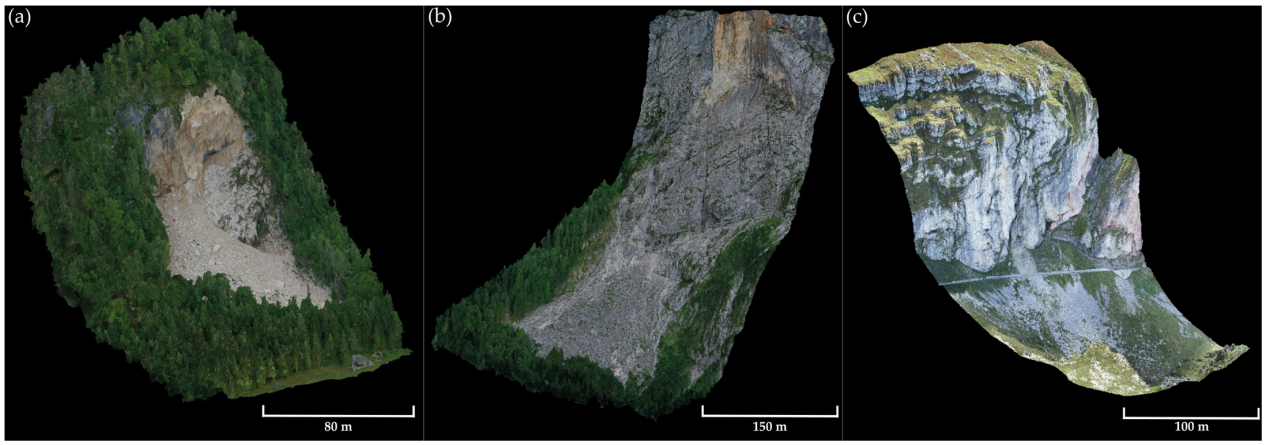


**Figure 2.** Three-dimensional representation of rockfall study sites: (**a**) Kekec, (**b**) Krnica, and (**c**) Mangart.

The Krnica rockfall occurred in 2007 from a steep rock wall and is situated approximately at 1465 m of altitude. The rockfall source area consists mostly of layers of bedded dolomite and limestone (Anisian–Ladinian; Triassic). The rocks diminished underlying parts of the forest stands, and the entire runout area of the rockfall covers approximately 50,000 $m^2$, with the furthest rocks stopped at an altitude of 1090 m. In the immediate vicinity of the rockfall deposits, there are hiking trails and a mountain hut. The rockfall Kekec is situated in Trenta valley, and it originated from a 10 to 50 m high rock cliff, represented by Daschstein limestone. Two larger events occurred at this rockfall in the last decade: one in 2012 and another in 2020. The rockfall runout has an area of approximately 4800 $m^2$. The events only affected the underlying forest stand, but further events could potentially endanger the residential houses next to it. The sources of the Mangart rockfall also originate from a 50- to 60-m-high steep rock wall, and it is characterized by platy and bedded micritic and crinoid limestone with chert (Malm) from the Jurassic period [42–44]. After the rockfall event, in 2013, the road that is situated directly below the source and was affected by the event was closed due to safety reasons. The runout Mangart rockfall has an area of 13,000 $m^2$.

### *2.2. Photogrammetric and LiDAR UAV Surveys*

At each study site, two UAV surveys were carried out. Photogrammetric surveys were performed with DJI Mavic 2 Pro [45] (Figure 3a). The UAV weighs 907 g, has a diagonal distance of 354 mm, and can fly up to 31 min in conditions without wind. A camera that is mounted on it is 1-inch in size, has 20 million effective pixels, a field of view (FOV) of about 77° 33 mm (28 format equivalent), an aperture of f/2.8–f/11, and a shooting range from 1 m to ∞. The size of the still image is 5472 × 3648. LiDAR surveys were performed with a DJI Matrice 600 Pro [46]; the UAV has a diagonal wheelbase of 1133 mm and a maximum takeoff weight of 15.1 kg. On this UAV, a YellowScan Surveyor Ultra (YellowScan, Saint-Clément-de-Rivière, France) [47] LiDAR system was mounted (Figure 3b). The scanner weighs 1.32 kg and has a size of 16 × 10.3 × 13.8 cm. It enables a laser range of 140 m (at 10% of target reflectivity), 640k shots, and 3 echoes per second.

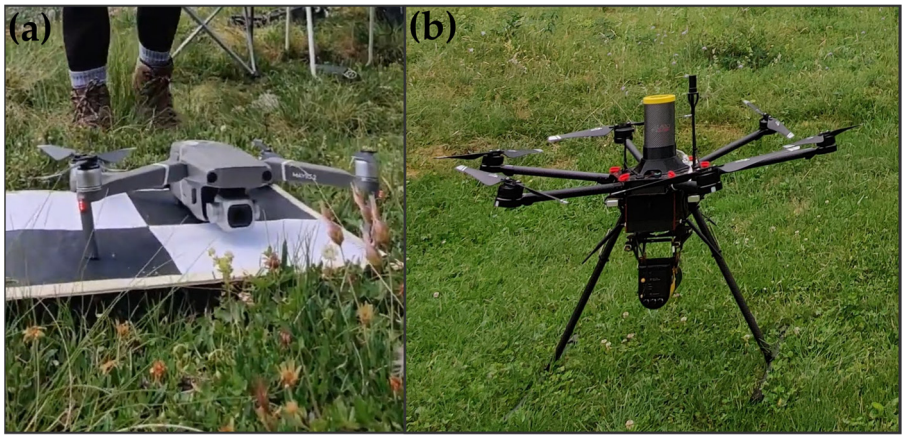


**Figure 3.** (**a**) DJI Mavic 2 Pro was used for photogrammetric surveys, and (**b**) DJI Matrice 600 Pro with LiDAR sensor YellowScan Surveyor Ultra was used for LiDAR surveys.

The UAV surveys were carried out on the following dates: 15 July 2021 at Kekec rockfall, 20 July 2021 at Krnica rockfall, and 21 July 2021 at Mangart rockfall. UAV missions were planned with UgCS Ground Station Software [48] so that the UAV was following the terrain. The terrain raster was derived from the LiDAR data of Slovenia in resolution 1 × 1 m [49]. The flights were planned with 80% frontal and 60% side overlap at the flying height above the terrain of 80 m. The missions were planned in a parallel and cross-grid flight pattern (Figure 4). Pictures were taken at two angles, 65°, and 85°, in order to obtain a more accurate representation of terrain and individual rock deposits [50]. LiDAR surveys were conducted with a field of view (FOV) of 60°. Ground control points (GCPs) were set throughout the study sites before flights, and they are measured with a Leica Zeno20 (Leica Geosystems, St. Gallen, Switzerland) with GG04 Smart Antenna. The flight plans and locations of the GPCs are available in Figure 4.

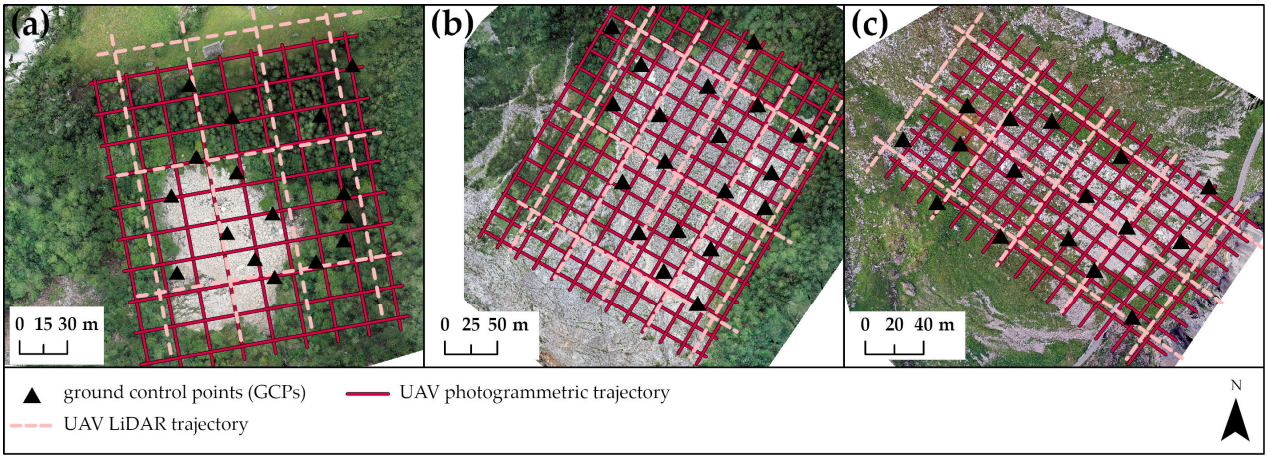


**Figure 4.** Flight plan for UAV photogrammetric and LiDAR survey for (**a**) Kekec site, (**b**) Krnica site, and (**c**) Mangart site. Orthomosaics were made based on the photogrammetric UAV survey.

### *2.3. Processing of UAV Data*

Images obtained with the photogrammetric UAV survey were processed with Pix4DMapper (Version 4.6.4) by Pix4D [51]. Bundle block adjustments were carried out by GCPs; the coordinate system for the horizontal geodetic datum was the Slovenia 1996/Slovene National grid with Slovenian Geodetic Datum 1996, while it was the Slovenian system SLOVRP2016 for the vertical geodetic datum. The configuration of the processing was as follows: initial processing was performed in full mode, and point cloud densification was made out of a 1/2 image scale with high point densities.

The LiDAR data were processed in the same horizontal and vertical system. The post-processing of trajectory was performed in the POSPac UAV [52], and the point cloud was further processed in the YellowScan CloudStation [53]. The strip adjustment of the flight lines was performed in TerraMatch by Terrasolid [54]. The densities of both photogrammetric and LiDAR point clouds are available in Table 1.

**Table 1.** The average density of the photogrammetric and LiDAR point cloud in different test sites.

| Average Density (Points per $m^2$) | Kekec | Krnica | Mangart |
|---|---|---|---|
| photogrammetric point cloud | 603 | 673 | 605 |
| LiDAR point cloud | 637 | 690 | 577 |

### *2.4. Selecting Rocks for Rock Dimension Survey*

In order to obtain reliable modeling results, it is important to obtain a representative sample of rocks that would reflect the mean dimensions of rocks in the rockfall runout zone for application in rockfall simulations.

In this study, a methodology based on energy line angles was used in order to select the rocks that were used as inputs into the rockfall model. Energy line angles (Figure 5) were first described by Heim [55], and it has since been used widely in different rockfall applications [56,57]. The energy line is a line defined by angle *ß* between the horizontal plane and a fictive line that is drawn from the top of the rockfall release area and the maximum stopping point. The *ß* angle is a feature that can be measured on the field and represents a rough statistical estimation of the rockfall's runout distance. The energy line principle assumes that the kinetic energy of a falling rock at a given point equals the potential energy at a given point. The magnitude of the angle depends on the hazard type, the mass component (e.g., type of rockfall source area, geology, geometrical shape, and size of the falling rocks), and on the relief (e.g., curvature, roughness, and steepness of the slope).

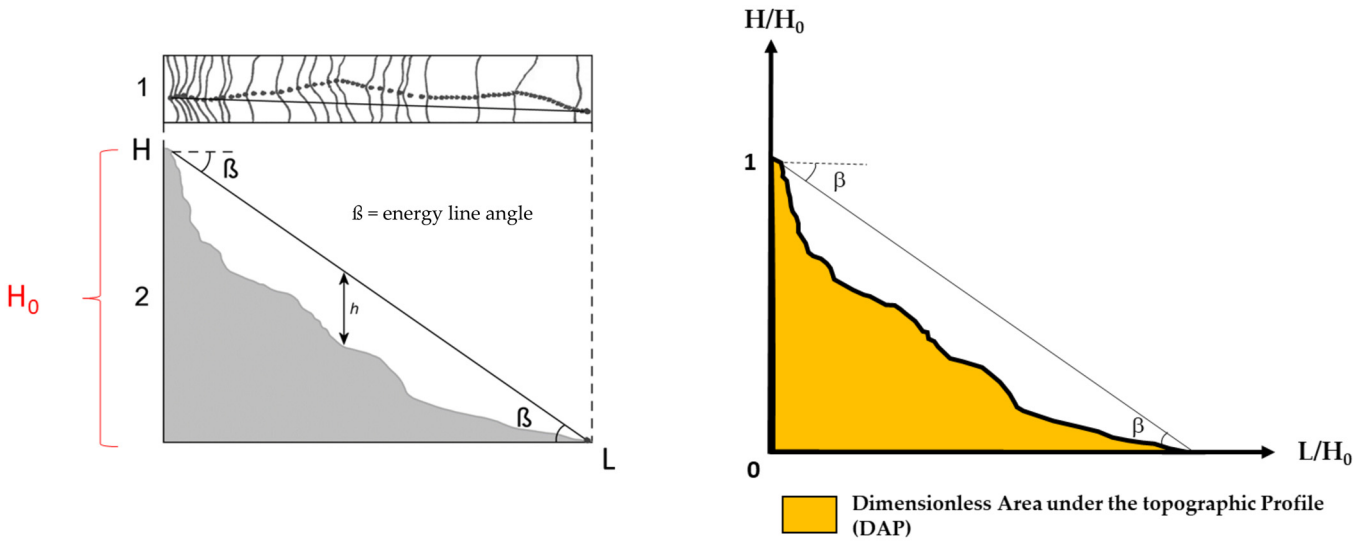


**Figure 5.** Conceptualization of energy line angle (*ß*) and dimensionless area under the topographic profile (DAP). $H_0$ is the change in the altitude based on the travel rock trajectory. *L* marks the length of the profile.

Field observations show that the magnitude of the angle is within a certain range and above certain limits with little variations. Therefore, it is possible to estimate the runout length of a rockfall event, if the rockfall source is known. Based on the more than one-hundred single rockfall events, the energy line angle is almost systematically greater than 24–26°; it can exceed 45° and reach nearly 60° in particular cases (e.g., subvertical cliffs

without long slopes). The value of the energy line angle will depend on the morphology of the surface; therefore, INRAE and BRGM [58] compiled an inventory of rockfall events and developed tools to obtain energy line angles that correspond to the individual surface slope's characteristics. In order to compare the morphology of various topographic profiles, Levy et al. [59] defined the dimensionless areas under the topographic profile (DAP) (Figure 5) that will only provide the change in length/height ($L/H_0$).

To validate this model's concept, a database on past rockfall events needed to be expanded. The authors of this method collected over 2800 events [60], and the databases were later enriched within the ROCKtheALPS project (Interreg-Alpine Space project), where more than 3600 events across the Alps were added [14,61]. The distributions of rock deposits and energy line angles were statistically quantified using the following: (i) non-linear regression, (ii) transformation of the variables for reductions into classic linear regressions, (iii) regression on extreme quantiles (with power transformation), and (iv) the calibration of the probability law of the logit-normal type.

Following these statistical evaluations, an ELANA mapping tool was developed [60]. ELANA is used to spatially map the probability of rockfall propagations in 2D. It uses DTM with a defined source area, and it obtains the values of energy line angles for high, medium, and low rockfall hazard risks from the proposed empirical laws. The software interpolates profiles around each starting pixel in order to determine the location of rockfall propagation limits for each profile. In order to limit the computation, this operation is performed for the pixels of the source area that are classified as "upstream", and then, the "downstream" pixels are located directly downstream of the source area pixel. The calculation starts with respect to the direction of the greatest slope around each "upstream" pixel by steps of 1°. The selection of direction is performed around the steepest slope within a cone of $\alpha/2$ ($\alpha$ defined by the user), and for the slope values, they are greater than 26°. The topographic profiles are interpolated from the source area for all directions and with a horizontal discretization of the grid cell's size.

At each point of the profile, the probability of rockfall propagation events is specified. The probability is dependent on the probability of there being a departure from the source area (Pd) and the probability of propagation (Pp) [58]. The final results are fixed on the rockfall probability that presents the worst-case angle value for all profiles intercepting the pixels. Based on the rockfall activity, three homogeneous probability zones are defined [58]: (i) high (at least one rockfall event every year), (ii) medium (rockfall event every 10 years), and low (rockfall events every 100 years).

Based on the profiles of rockfalls in this study (Figure 6), the ELANA tool was used to obtain values of *ß* for each site for high, medium, and low rockfall propagation probabilities (Table 2).

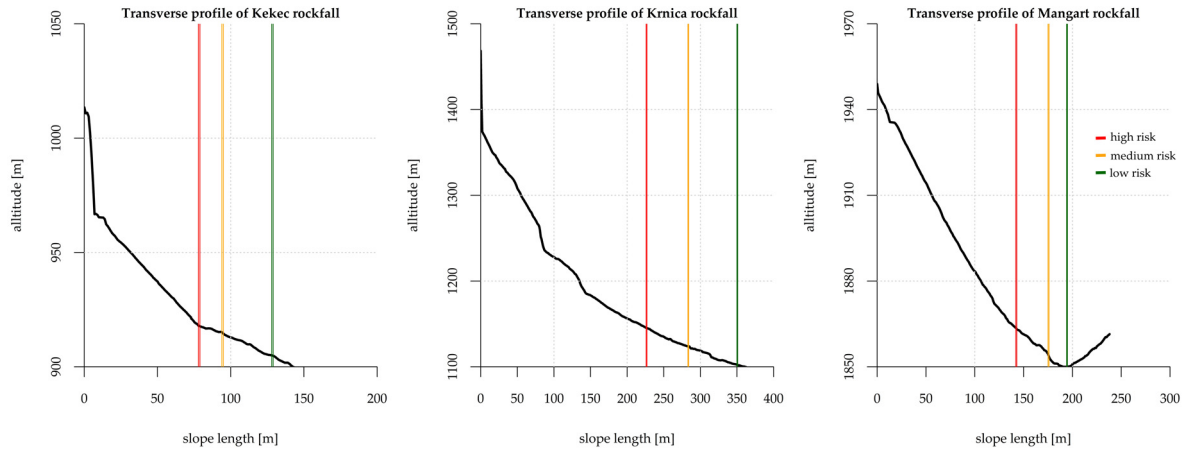


**Figure 6.** Transverse profile of rockfall study sites (Kekec, Krnica, and Mangart) used in the ELANA tool to calculate energy line angle ß (°) for each hazard risk zone.

**Table 2.** The values of energy line angle *ß* (°) were calculated for each hazard risk zone.

| | Kekec | Krnica | Mangart |
|---|---|---|---|
| High hazard risk | 49.34° | 52.17° | 30.00° |
| Medium hazard risk | 45.82° | 47.72° | 28.00° |
| Low hazard risk | 41.03° | 43.62° | 26.00° |

To determine which rock deposits were selected in the analysis, we created a buffer area of 0.5 m at each hazard zone (Figure 7) and performed a rock dimension survey of all rocks that were located within this zone or were touching it. The identification of rocks was performed based on the orthomosaics and hill shades provided in the UAV surveys. Based on the calculated high-, medium-, and low-risk zones and the actual locations of the rock deposits, the actual rock deposits were located only in high and medium-hazard risk zones, while the probability of being deposited at low-hazard risk zones was not realized. Consequently, the rocks were only surveyed within high and medium-hazard risk zones.

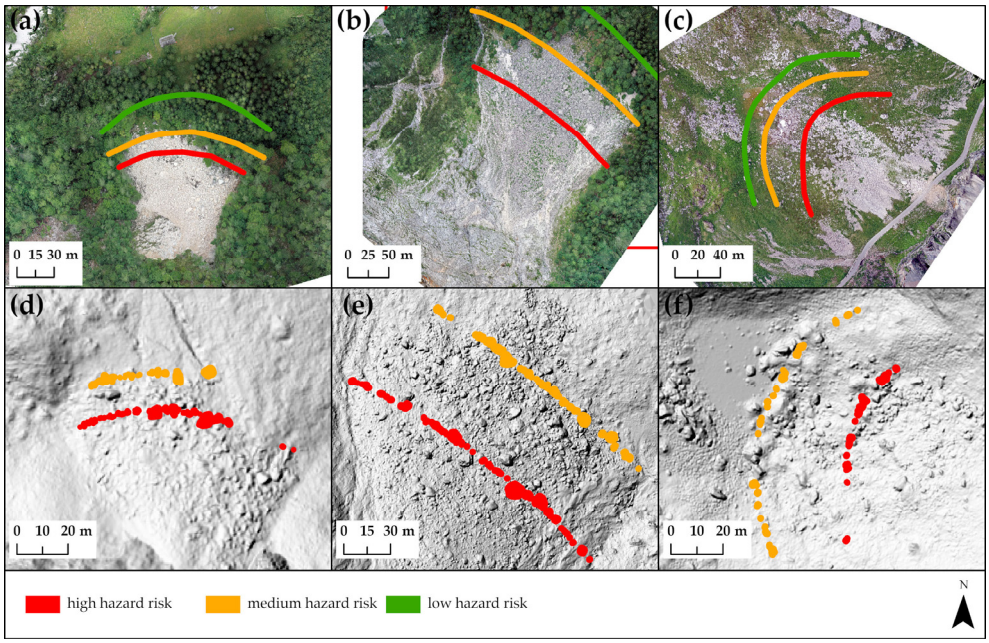


**Figure 7.** Locations of hazard risk zones and locations of rock deposits that were determined for the measurement of rock dimensions with three methods. (**a**,**d**) Kekec site, (**b**,**e**) Krnica site, and (**c**,**f**) Mangart site.

### *2.5. Measuring Dimensions of the Rocks with Three Methods*

The dimensions of rock deposits were measured with three different methods: (i) directly on the field with a measuring tape, (ii) in photogrammetric point clouds and (iii) in LiDAR point clouds.

The first measurement was performed on the field based on the identified rock deposits within each hazard zone (Section 2.4). Before the measurements, we performed a UAV survey and obtained an orthomosaic. Based on this orthomosaic and the location of the high, medium, and low hazard risks, we digitalized the outlines of the rocks that were located within individual zones. This rock mask was used as the basis for the field survey of rock dimensions. When conducting measurements on the field, we eliminated the rocks that were buried or covered by other rocks so that only the rocks with all three dimensions available for measurement (length, width, and height) were included in the study. The measurements on the field were performed with a measuring tape, and for each dimension, we aimed for the maximum geometrical length, which was estimated based on the visual inspection.

The measurements in both photogrammetric and LiDAR point clouds were performed in two steps. Firstly, each rock was extracted from the common point cloud. This was carried out with segmentation in the CloudCompare software [61]. In this step, the outlier points were eliminated in order to reduce potential overestimations of dimension calculations. Secondly, the dimensions of single rocks were automatically extracted with an algorithm named minimum bounding volume in ArcGIS Pro [62]. This algorithm creates multipatch features, which represent the volume of space occupied by a set of 3D features (Figure 8). To obtain three dimensions of the individual rocks, an envelope method was used since it provides the XYZ extent of objects [63,64]. The dimensions are an expression of the maximum extent of a three-dimensional object. The following approach was used since the inputs into the rockfall model must have the maximum dimensions (see Section 2.6). Moreover, from the calculation point of view, these procedures were not demanding nor time-consuming, and for these reasons, they are appropriate for the analyses of rockfall activity at the slope level by different experts.

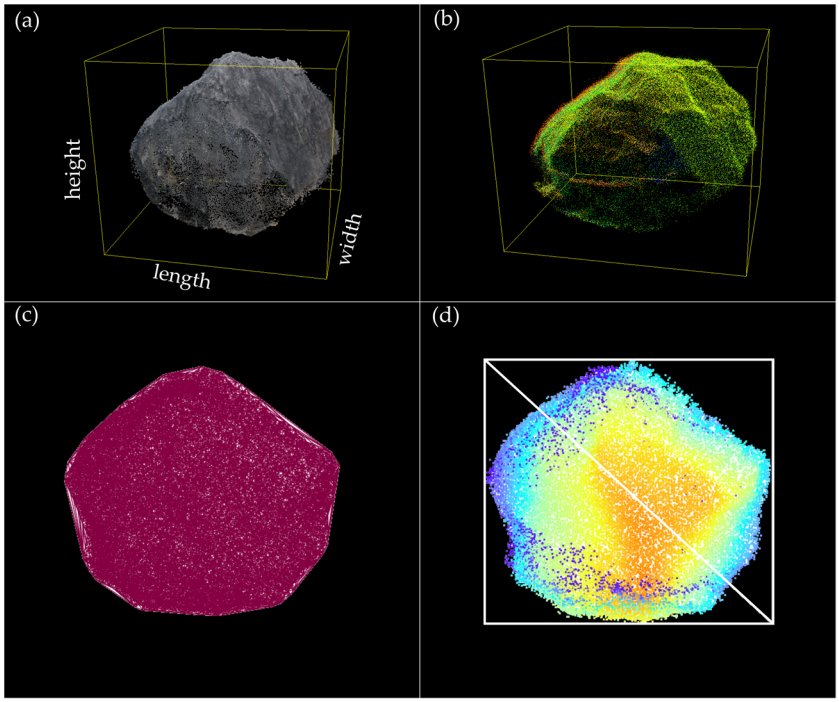


**Figure 8.** (**a**) Extracted rock deposit from the photogrammetric point cloud with markings on how rock dimensions were measured; (**b**) the same rocks were extracted from the LiDAR point cloud; (**c**) representation of the point cloud as a multipatch, simulating the shape of the rock; and (**d**) representation of the point cloud with elevation and markings of the envelope method from the minimum bounding volume algorithm.

### *2.6. Modeling Rockfall Runout Zones with Rockyfor3D*

Rockyfor3D [11] is a probabilistic process-based rockfall trajectory model that calculates trajectories of single falling rocks in three dimensions (3D). The model can be used for regional-, local- and slope-scale rockfall simulations. The rockfall trajectory is simulated as a 3D vector by calculating the sequences of classical parabolic free fall via the air and rebounds on the slope's surface, as well as the impacts against trees. In the model, rolling is represented as a sequence of short-distance rebounds. The inputs consist of ASCII grid layers that define topography and the slope's surface characteristics. The authors of the model argue that the preferred resolution of the raster input is between 2 × 2 m and 10 × 10 m [11,65].

The initial settings of the model require defining the number of simulations within one model, the variation in rock volume (in %), and the initial fall height (in meters). The number of simulations defines the number of individual trajectories that will be simulated

from each rockfall source cell [11]. As recommended by the authors of the model, the number of simulations was always set to 1000 [11]. The variation in rock volume represents the percentages within the three rock dimensions that are randomly varied during each single simulation of the trajectory. The value is by default set to 0%, and it was used in the case of all study areas. The focus of the study was on the input dimensions of the rocks, and the changes in the variation of rock volume also do not influence the final modeling results as much as the initial fall height or dimensions of rocks [66]. With additional fall height, we define the height in meters above DTM from which the rocks will be released initially, and it can be set to a maximum value of 50 m. The initial fall height with all studied rockfalls was set to 50 m since they all originate from rockfall walls, which exhibit higher values higher than 50 m.

Rock dimensions, located within the rockfall area [67], in the model are presented by height, width, and length in each rockfall source raster cell. These values represent the average value of each dimension [57]; therefore, the averages of all measurements for each site were calculated separately for each method of measurement (measurements on photogrammetric point cloud, LiDAR point cloud, and field measurements). The values are presented in Table 3. The input dimensions are further within the model used for calculating the block volume and it's mass. In order to analyze the differences between methods, the model was separately run three times for each site depending on each measurement method.

**Table 3.** Mean values of rock dimensions (width, length, and height) calculated for all measurement methods.

| Rock Dimensions Measurement Method | Kekec Site | | |
|---|---|---|---|
| | **Width (m)** | **Length (m)** | **Height (m)** |
| Photogrammetric point cloud | 1.1 | 1.4 | 1.1 |
| LiDAR point cloud | 1.2 | 1.4 | 1.2 |
| Field measurement | 1.0 | 1.3 | 1.0 |
| | **Krnica Site** | | |
| Photogrammetric point cloud | 1.3 | 1.5 | 1.2 |
| LiDAR point cloud | 1.4 | 1.7 | 1.4 |
| Field measurement | 1.2 | 1.5 | 1.2 |
| | **Mangart Site** | | |
| Photogrammetric point cloud | 0.7 | 0.8 | 0.6 |
| LiDAR point cloud | 0.7 | 0.9 | 0.7 |
| Field measurement | 0.6 | 0.9 | 0.6 |

Rock density is defined for rocks in the rockfall source area, and it is expressed in $kg/m^3$. Since limestone is the prevailing rock in the source area of all studied rockfalls, a mean density of 2500 $kg/m^3$ was used, as recommended by the authors [57]. The prevailing rock dimension was set to rectangular dimensions [66].

The resolution of the digital terrain model (DTM) comprised grid cells of 2 × 2 m as the experience of the authors shows that higher-resolution grid cells do not necessarily improve the quality of the results [11,65]. The source of DTM was the LiDAR scanning of Slovenian terrain [49]. The rockfall source area was determined on the DTM using hill shade, past orthophoto imagery, and orthomosiacs obtained by UAV surveys in this study.

The surface roughness is in the Rockyfor3D model, and it is represented by three raster maps (rg70, rg20, and rg10). These rasters represent the rocks laying on the ground that form obstacles for falling rocks. These rocks are defined by polygons that contain a value of the surface roughness that expresses the size of the material (the height of

a representative obstacle in meters—MOH) covering the surface's slope relative to the downward direction of the slope. One raster represents a MOH of 70% with respect to the homogenous area, the second raster represents 20%, and the third raster represents 10%. The delimitation into homogeneous zones of surface roughness was performed in combination with fieldwork and orthomosaics, which were obtained with the UAV survey. The defined surface roughness areas and their values are presented in Figure 9 and Table 4.

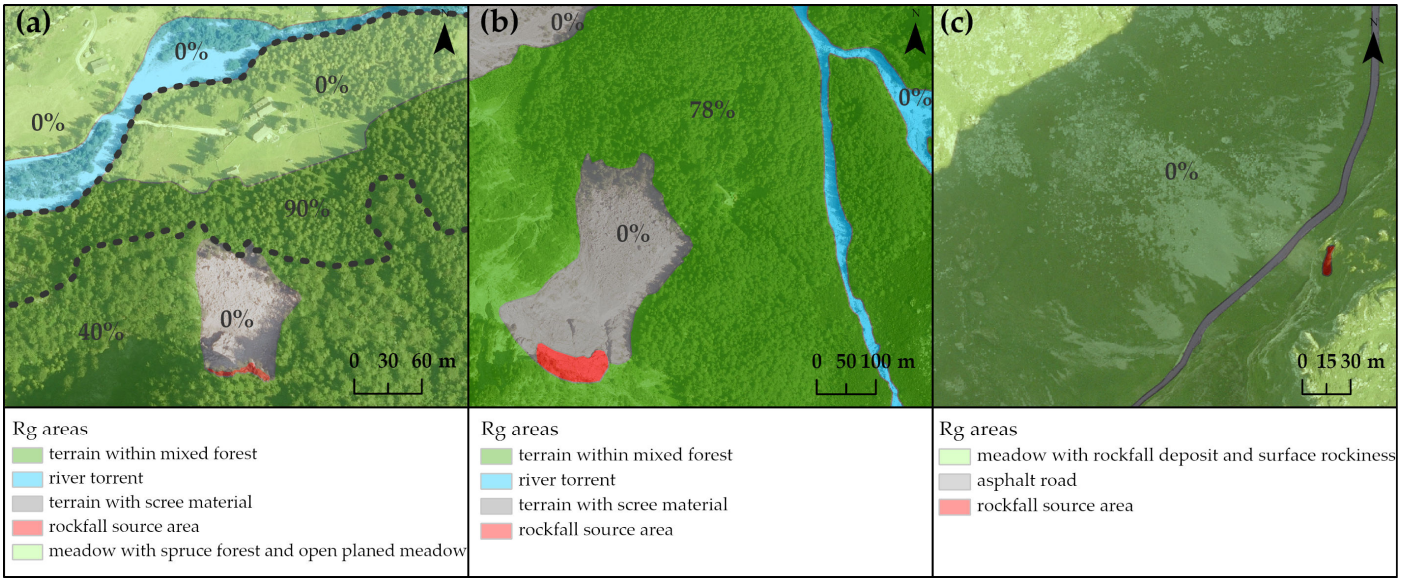


**Figure 9.** Surface roughness (rg) surface slope types delineated into rg subareas for the (**a**) Kekec site, (**b**) Krnica site, and (**c**) Mangart site. Percentage (%) values at each subarea represent the percentage of conifers in that subarea.

**Table 4.** Surface roughness (rg) areas with soil types defined at each study site.

| | **Kekec** | | | |
|---|---|---|---|---|
| | **Rg70** | **Rg20** | **Rg10** | **Soil Type** |
| Terrain with scree material | 0.13 | 0.15 | 0.25 | Type 4 |
| Terrain within mixed forest, characterized by rockfall deposits, surface rockiness, laying logs and stumps | 0.30 | 0.33 | 0.20 | Type 4 |
| Meadow with spruce forest and open-planed meadow | 0 | 0 | 0 | Type 1 |
| River torrent | 0.17 | 0.32 | 0.53 | Type 4 |
| | **Krnica** | | | |
| Terrain with scree material | 0.12 | 0.13 | 0.18 | Type 4 |
| Terrain mixed forest characterized by surface rockiness, laying logs, and stumps | 0.10 | 0.35 | 0.15 | Type 4 |
| River torrent | 0.25 | 0.50 | 0.90 | Type 4 |
| | **Mangart** | | | |
| Meadow with rockfall deposit and surface rockiness | 0.05 | 0.10 | 0.20 | Type 4 |
| Asphalt road | 0 | 0 | 0 | Type 1 |

The model's simulations can also enable modeling with protective forest effects. The Mangart site is not covered by forests, while the other two locations have forests present in the runout zone. Therefore, simulations at these two sites required the preparation of two additional inputs. The first input is a raster that represents the percentage of conifers in the forest, and the second input is a text file containing the locations of each tree with the corresponding diameter at breast height (DBH) in cm. The mean percentage of conifers

was obtained from the forest stand maps of the Slovenian Forest Service [68], and the delineation into zones of different percentages was carried out along with orthomosaic operations and field inspections (Figure 9). At the Krnica site, all present forests were placed in one zone, which represents 78% of coniferous tree species (*Picea abies* Karst., *Larix decidua* Mill., *Abies alba* Mill. and *Pinus sylvestris* L.). At the Kekec site, two zones can be identified: a zone with 40% of conifers and a zone with 90% of conifers (*Picea abies* Karst., *Abies alba* Mill.).

### *2.7. Evaluation of the Input Parameters and Modeling Results*

#### 2.7.1. Comparison of Rock Dimensions and Volumes

In order to test if there are statistically significant differences between rock dimensions and the volumes of the three measurement methods, a one-way multivariate analysis of variance (MANOVA) between the groups was used. MANOVA assumes that the centroids are the same for all groups, meaning that they do not differ significantly. Since none of the assumptions for a parametric MANOVA were met (a multivariate outlier detected; multivariate normality—$p < 0.05$; multicollinearity—correlation > 0.09; homogeneity of covariance—$p > 0.05$; homogeneity of variance assumption > 0.05), and a non-parametric multivariate analysis of variance (NPMANOVA) was used.

The analysis was carried out using R software [69], namely using function adonis2. adonis2 is a permutational multivariate analysis of variance that uses distance matrices (based on principles by McArdle and Anderson [70]). The analysis of variance is performed by using distance matrices among the sources of variations and by fitting linear models (e.g., factors) to distance matrices. The analysis used a permutation test with pseudo-F-ratios. The function can perform sequential, marginal, and overall tests.

The results of rocks' volumes were evaluated by using Pearson's correlation analysis and the Passing–Bablok regression [71] analysis in R. The differences between any combination of rock measurement methods were presented as a Bland–Altman plot. The Passing–Bablok regression model is used for comparing modeling methods. In the case of this study, a comparison is made of the different measuring methods used for evaluating rock dimensions. This regression model was used since it applied nonparametric regression as no parametric form is assumed for the relationship between the predictive and dependent variables.

It is not sensitive toward outliers, and it assumes that the measurement errors in all methods have the same distribution [72]. The requirements of the method are continuously distributed measurements and a linear relationship between the compared methods. The final result is the calculated regression line equation from the two compared data sets. In the analysis, each pair of the method was compared; a linear equation, Pearson's correlation coefficient, and 95% confidence intervals (95% CI) were determined for each comparison.

#### 2.7.2. Maximum Runout Zones

The modeled maximum runout zones between the different methods of obtaining the dimensions of rock input data were evaluated using a Rockyfor3D simulation model and examining the propagation probability. This modeling result represents the most realistic spatial distribution of the current rockfall event, and it is used for the calculation of spatial calculation probability, which is often used in rockfall hazard analyses [11].

To compare the modeling results of rockfall runout areas to an actual rockfall area, goodness-of-fit (GOF) indexes [73] were used. GOF indexes are based on pixel-by-pixel comparisons between the observed rockfall area (OR) and predicted rockfall area (PR), and the comparisons are made with rockfall modeling. Rockfall modeling is carried out by comparing OR and PR results in a binary map with positive values that correspond to the actual rockfall area and negative values that correspond to areas without rockfall areas. The combination of OR and PR results in four types of pixel results: (i) true positive—TP (correct prediction of the rockfall runout area: OR and PR); (ii) true negative—TN (correct prediction of areas with no rockfall runout areas: OR and PR); (iii) false positive—FP

(false prediction of rockfall runout areas on PR where it is not OR); (iv) false negative—FN (missed alarm—PR is mapped as no rockfall runout areas where there is actually OR). The presented indexes represent the basis of the concept of receiver operator characteristics (ROC) [74], which is used for assessing the model's performance by using the relation between benefits (TP) and costs (FP).

Formetta et al. [73] incorporated eight GOF indexes into the ROC system for the quantification of model performance. Žabota et al. [66] tested the use of these indexes for quantifying the modeling results of the rockfall propagation area, and they came to the conclusion that four of these indexes were most suitable for evaluation. These are as follows: success index (SI), distance to the perfect classification (D2PC), the average index (AI), and true skill statistics (TSS). In this research study, the same four indexes were used to evaluate the performance of the rockfall model. Equations for the calculation of these indexes are represented in Table 5.

**Table 5.** Definition of goodness-of-fit (GOF) indexes [73] used for the evaluation of rockfall runout zone modeled by three methods for measuring rock dimensions.

| Name | Definition | Range | Optimal Value |
|---|---|---|---|
| Success index (SI) | $SI = \frac{1}{2} \times ((TP/TP + FN)) + (TN/(FP + TN))$ | [0, 1] | 1.0 |
| Distance to the perfect classification (D2PC) | $D2PC = \sqrt{}((1 - TPR)^2 + (FPR)^2)$ | [0, 1] | 0.0 |
| Average index (AI) | $AI = \frac{1}{4} \times ((TP/(TP + FN)) + (TP/(TP + FP)) + (TN/FP + TN)) + (TN/FN + TN)))$ | [0, 1] | 1.0 |
| True skill statistics (TSS) | $TSS = ((TP \times TN) - (FP \times FN))/((TP + FN) \times (FP + TN))$ | [−1, 1] | 1.0 |

#### 2.7.3. Maximum Kinetic Energies and Passing Heights of Rocks

For the evaluation of maximum kinetic energies, we used rockfall results named maximum kinetic energies (E_95CI), and for the passing heights of rocks, a result called maximum passing heights (Ph_95CI) is used. In the model, the maximum kinetic energies represent the 95% confidence interval of all maximum kinetic energy in kJ recorded in each cell, and the maximum passing heights represent the 95% confidence interval of all maximum passing height values in meters, measured in the normal direction relative to the slope's surface. Both are calculated throughout the entire rockfall runout area, and they are used for the dimensioning process of rockfall protective measures [65].

In order to compare the results of different methods with respect to obtaining input rock dimensions, we extracted the values of both results from the locations of the measured rocks in all hazard risk zones. The results were statistically evaluated in the same way as for the rock volumes—by Pearson's correlation analysis and Passing–Bablok regression—while the differences between any combinations of rock measurement methods were shown by using a Bland–Altman plot.

## 3. Results

### *3.1. Comparison of Rock-Measuring Methods*

Figure 10 shows the boxplots for all measuring methods according to the width, length, and height of individual rocks. It can be observed that all three methods at all sites have similar distributions with respect to values and that the differences between the groups of methods are not large. The measurements of the LiDAR point cloud provide the largest values between the methods, while the field measurements are the lowest. The largest differences between the measurement methods are present in regard to the height. The results of the non-parametric one-way MANOVA test after implementing the *adonis* function show that there are no statistically significant differences between the centroids of different measuring methods with respect to rock dimensions ($p > 0.05$). With 999 permutations, a $p$-value of 0.610 was reported for Kekec, 0.442 was reported for Krnica, and 0.212 was reported for the Mangart site.

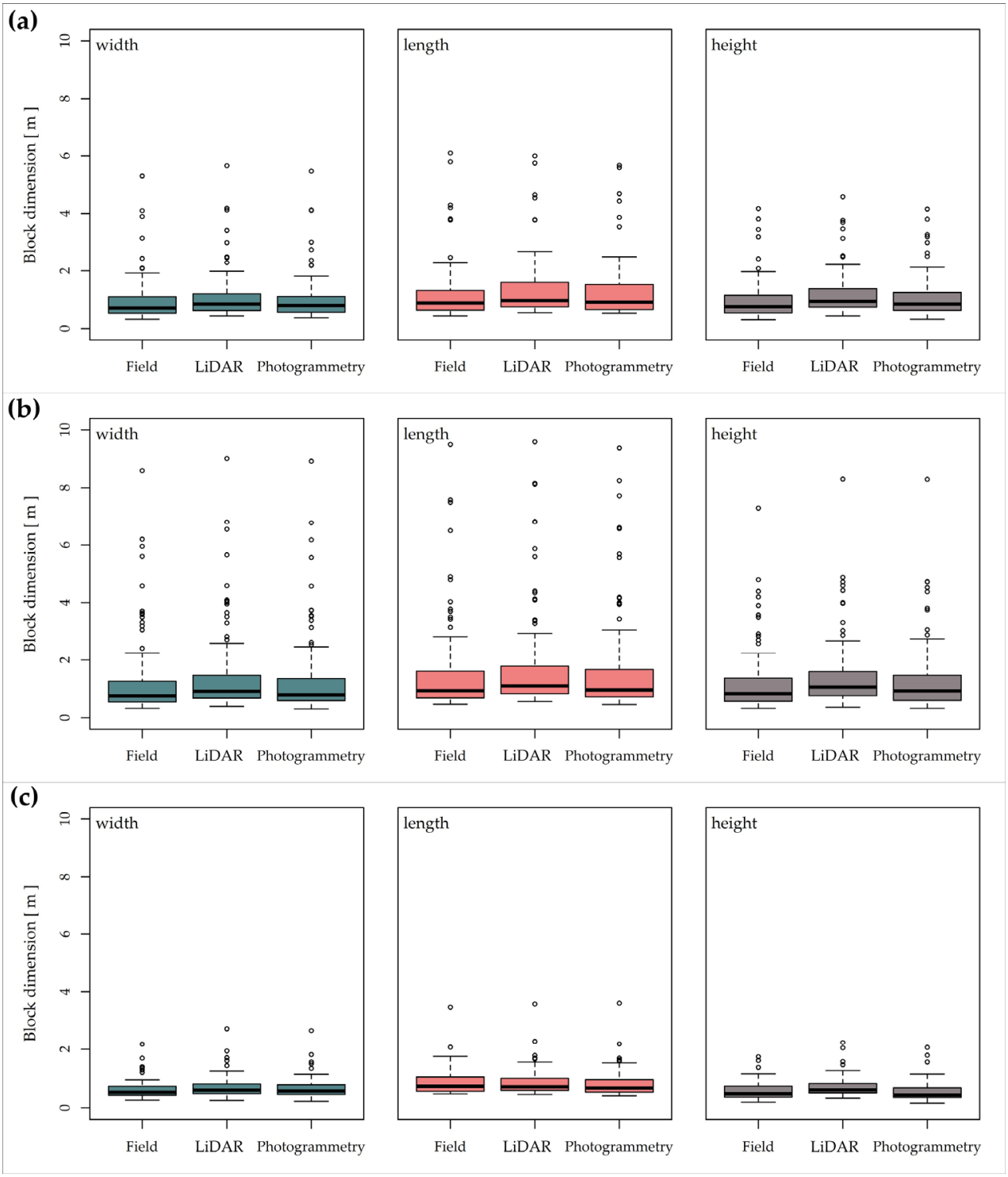


**Figure 10.** Boxplots for rock dimensions according to different measuring methods (field measurement, LiDAR point cloud, and photogrammetric point cloud) for (**a**) Kekec, (**b**) Krnica, and (**c**) Mangart.

When observing the results for rock volumes (Table 6), similar conclusions can be drawn. At all rockfall sites, measurements from the LiDAR point cloud provide the largest values, while values obtained with field and photogrammetry measurements were closer together. The range of measured values is similar with all three methods across all study sites.

**Table 6.** Statistical distribution of the rock volumes ($m^3$) for methods based on field measurements and measurements based on LiDAR and photogrammetric point cloud.

| Method | MIN | Q1 | Median | Q3 | MAX |
|---|---|---|---|---|---|
| **Kekec Site** | | | | | |
| Field | 0.06 | 0.13 | 0.28 | 1.11 | 82.20 |
| LiDAR | 0.08 | 0.26 | 0.52 | 1.61 | 79.09 |
| Photogrammetry | 0.06 | 0.42 | 0.42 | 1.15 | 70.11 |
| **Krnica Site** | | | | | |
| Field | 0.04 | 0.16 | 0.39 | 1.83 | 417.49 |
| LiDAR | 0.08 | 0.31 | 0.71 | 2.90 | 502.50 |
| Photogrammetry | 0.05 | 0.17 | 0.47 | 2.15 | 485.85 |
| **Mangart Site** | | | | | |
| Field | 0.03 | 0.06 | 0.16 | 0.35 | 9.21 |
| LiDAR | 0.04 | 0.10 | 0.21 | 0.49 | 15.25 |
| Photogrammetry | 0.01 | 0.05 | 0.13 | 0.32 | 13.81 |

The Passing–Bablok regression analysis shows a good agreement with all pairs of measuring methods at all sites, and Pearson's correlation coefficient (r) shows that these methods are highly correlated ($r > 0.987$, $p < 0.001$) (Figure 11). The intercept in all cases includes a value of 0, while the slope value is 1, proving that the differences between the compared methods are not statistically significant.

The Bland–Altman plot (Figure 12) reveals that the majority of compared rock volumes are located within the 95% CI, with only a few values standing out, while the mean differences between the measurement methods are close to 0.

### *3.2. Evaluation of Rockfall Propagation Probability*

The modeling results of the rockfall propagation probability are presented in Figure 13, where the modeled runout extents are mapped against the actual runout extents. Visually, the differences are small, and they are noticeable particularly in individual trajectories, especially at the Kekec site. However, overall, the modeling extents do not differ significantly between the measurement methods.

After the statistical evaluation of the results with GOF indexes (Table 7), it can also be concluded that the differences between the measurement methods are small. Overall, slightly more precise results are presented with LiDAR point cloud measurements when observing the Kekec and Krnica sites, while the measurements from the photogrammetric and LiDAR point clouds represent almost identical results at the Mangart site. Results based on field measurements represent the worst modeling results, but the differences relative to other methods are almost negligible. The comparison of the modeled rockfall area is performed only to the actual extent that represents the extreme outline for all three sites; individual rocks can also travel further than this extent.

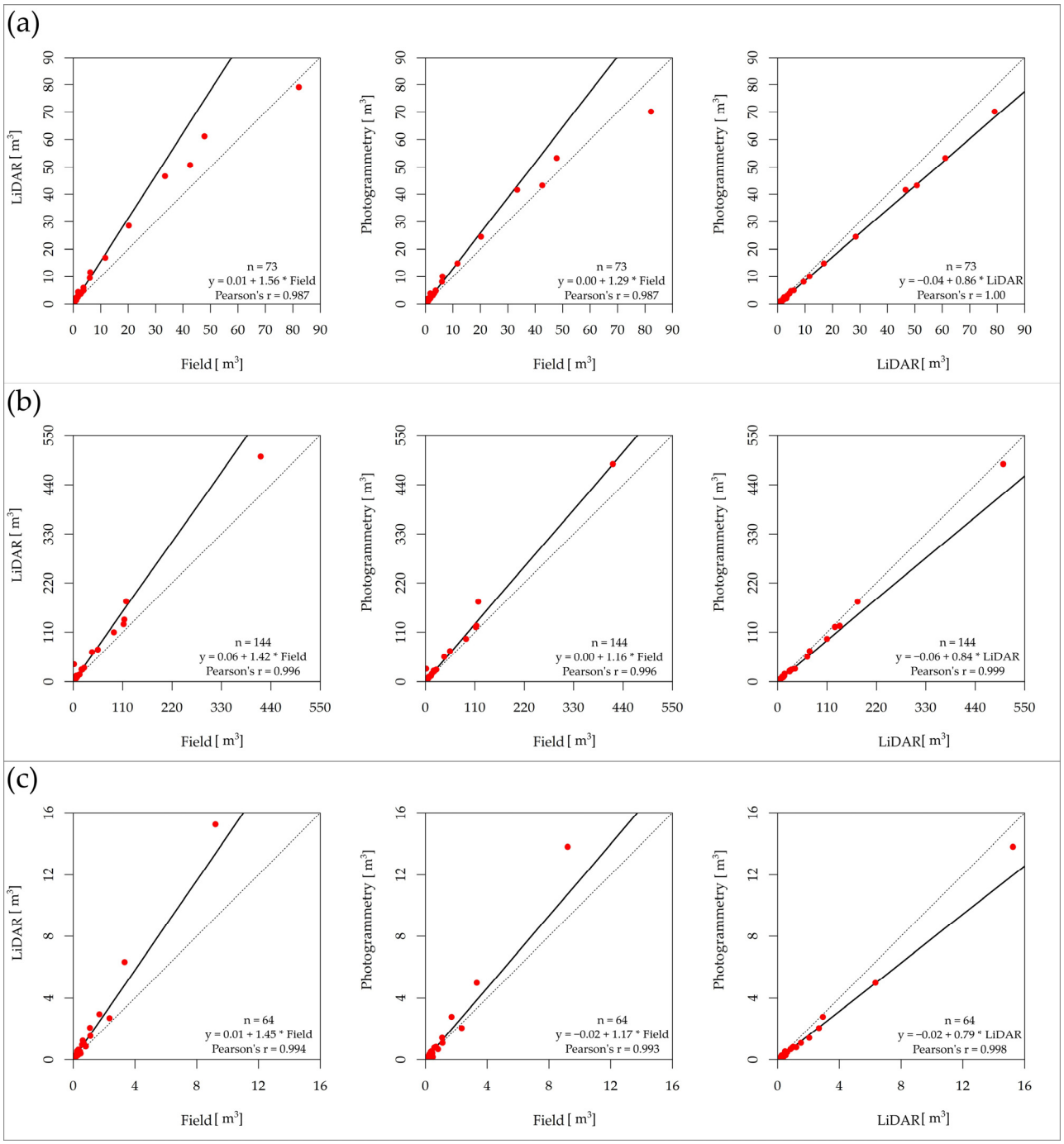


**Figure 11.** Passing–Bablok regression analysis for rock volumes ($m^3$) for different pairs of measuring methods (field measurement, LiDAR point cloud, and photogrammetric point cloud) for (**a**) Kekec, (**b**) Krnica, and (**c**) Mangart.

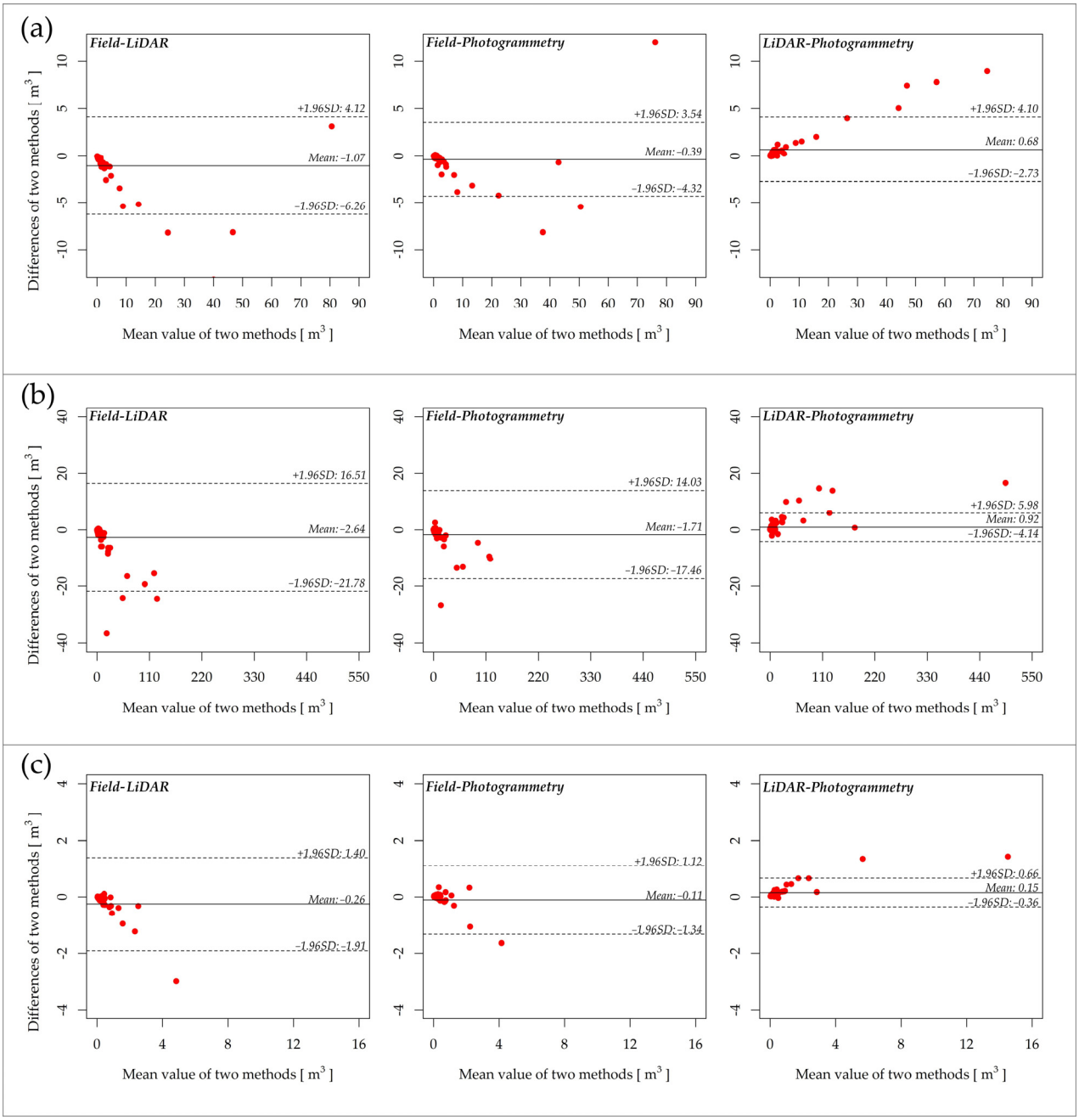


**Figure 12.** Bland–Altman plot for the differences in rock volumes ($m^3$) between any combination of rock measurement methods (field measurement, LiDAR point cloud, and photogrammetric point cloud) for (**a**) Kekec, (**b**) Krnica, and (**c**) Mangart.

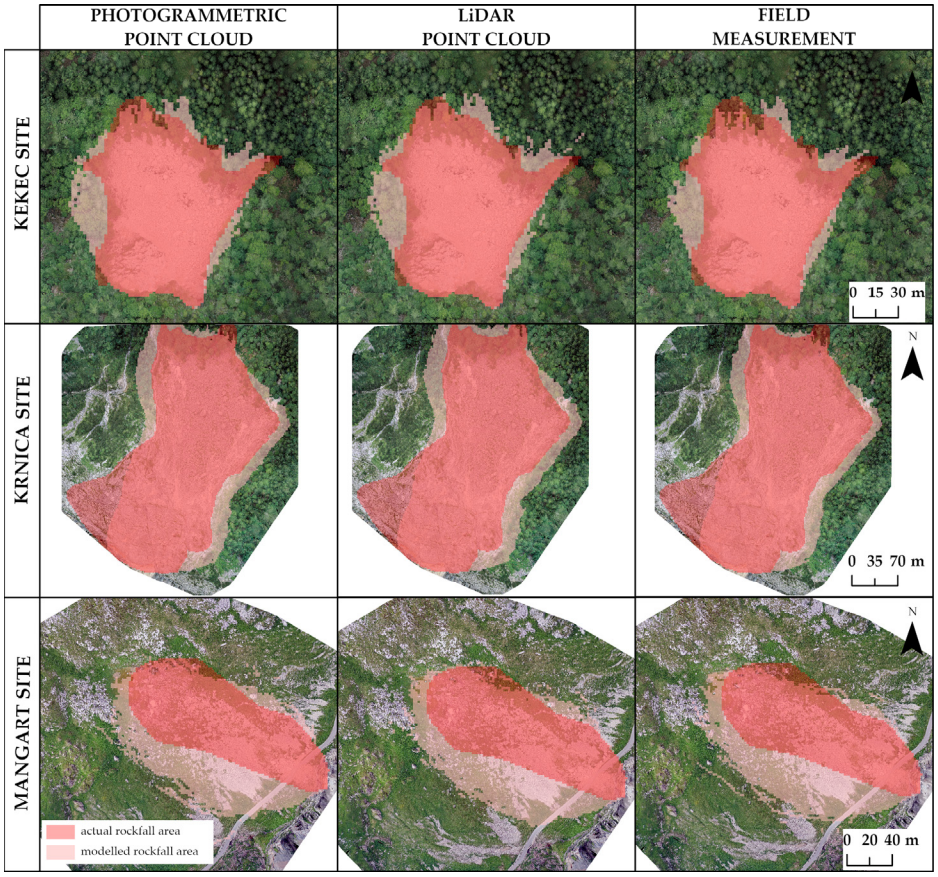


**Figure 13.** Modeling results for the maximum runout zone—propagation probabilities for Kekec, Krnica, and Mangart sites.

**Table 7.** Results modeling evaluated using goodness-of-fit (GOF) indexes: success index (SI), distance to the perfect classification (D2PC), average index (AI), and true skill statistics (TSS).

| **Kekec** | **SI** | **D2PC** | **AI** | **TSS** |
|---|---|---|---|---|
| LiDAR point cloud | 0.97 | 0.04 | 0.94 | 0.94 |
| Photogrammetric point cloud | 0.97 | 0.05 | 0.94 | 0.93 |
| Field measurement | 0.95 | 0.08 | 0.94 | 0.90 |
| **Krnica** | **SI** | **D2PC** | **AI** | **TSS** |
| LiDAR point cloud | 0.94 | 0.10 | 0.92 | 0.88 |
| Photogrammetric point cloud | 0.94 | 0.11 | 0.92 | 0.87 |
| Field measurement | 0.94 | 0.11 | 0.93 | 0.87 |
| **Mangart** | **SI** | **D2PC** | **AI** | **TSS** |
| LiDAR point cloud | 0.97 | 0.05 | 0.88 | 0.93 |
| Photogrammetric point cloud | 0.97 | 0.05 | 0.88 | 0.93 |
| Field measurement | 0.95 | 0.07 | 0.87 | 0.91 |

### *3.3. Evaluation of Maximum Kinetic Energies*

Table 8 shows the maximum kinetic heights for each site and rock-measuring method. It can be observed that the modeling results based on LiDAR measurements achieved maximum kinetic energy values, and the measurements are statistically and significantly different from photogrammetry and field measurements. Field measurements achieved the lowest kinetic energies among all measurement methods, while the values from photogrammetry measurements fall within the mid-range. The differences are the lowest at the Mangart site, while the largest differences were observed at the Krnica site as the results surpassed the median values from the field point cloud by more than 1000 kJ.

**Table 8.** Statistical distribution of maximum kinetic energies (kJ) for methods based on field measurements and measurements based on LiDAR and photogrammetric point cloud methods.

| Method | MIN | Q1 | Median | Q3 | MAX |
|---|---|---|---|---|---|
| **Kekec Site** | | | | | |
| Field | 365.56 | 492.96 | 570.93 | 642.31 | 864.29 |
| LiDAR | 656.43 | 829.35 | 878.36 | 981.71 | 1188.03 |
| Photogrammetry | 523.49 | 654.23 | 725.28 | 804.34 | 988.73 |
| **Krnica Site** | | | | | |
| Field | 808.88 | 1206.22 | 1465.79 | 1664.92 | 1987.75 |
| LiDAR | 1276.23 | 1968.60 | 2424.06 | 2817.82 | 3327.47 |
| Photogrammetry | 927.40 | 1355.30 | 1607.60 | 1860.31 | 2240.49 |
| **Mangart Site** | | | | | |
| Field | 10.22 | 162.20 | 203.34 | 236.19 | 611.81 |
| LiDAR | 130.55 | 234.46 | 275.24 | 336.22 | 713.57 |
| Photogrammetry | 71.74 | 166.09 | 211.23 | 232.13 | 584.62 |

The Passing–Bablok regression (Figure 14) analysis confirms that there is no agreement with all pairs, especially when comparing the field and LiDAR measurement methods since the intercept is the largest among all comparisons. Pearson's correlation coefficient showed that these methods are not strongly correlated ($r < 0.5$, $p > 0.001$); the coefficient is only high at the Krnica site. This confirms that the results of the regression can not only be assessed by using Pearson's correlation coefficient but the differences between the values must also be taken into account.

The Bland–Altman plot (Figure 15) shows that the mean differences of rock measurements are largely dispersed within the 95%CI and not close to 0, only confirming the large differences.

### *3.4. Evaluation of the Maximum Passing Heights*

Similar differences—as already discussed in previous sections outlining the results—can also be observed with maximum passing heights. The measurements with LiDAR point cloud achieved the highest passing heights with respect to the rocks, with field measurements possessing the lowest passing heights (Table 9). However, the differences here do not exhibit the same rates as with kinetic energies. At Mangart locations, the mean passing height is very close between all three measurements.

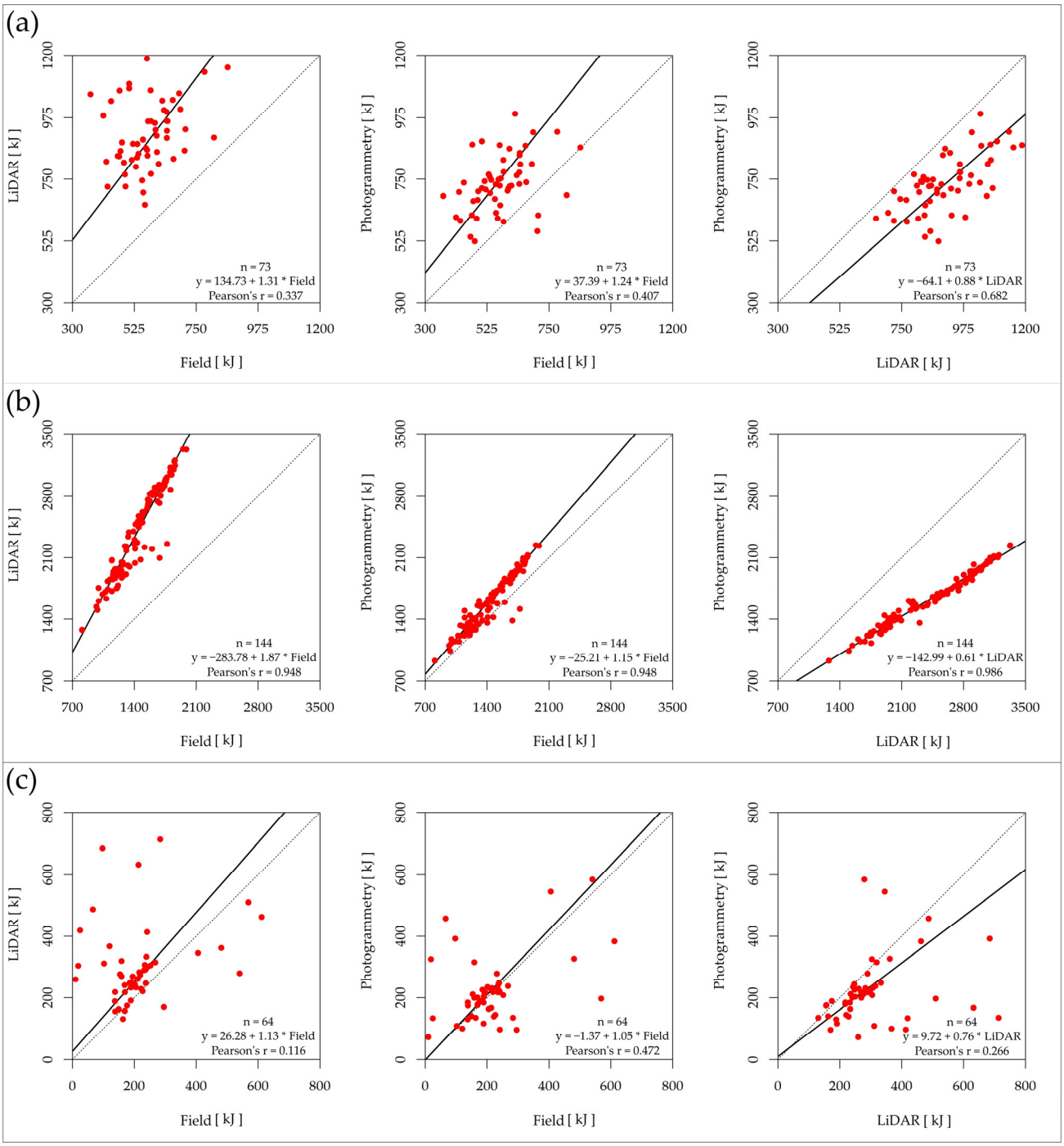


**Figure 14.** Passing–Bablok regression analysis for maximum kinetic energies (E_95CI) for different pairs of measuring methods (field measurement, LiDAR point cloud, and photogrammetric point cloud) for (**a**) Kekec, (**b**) Krnica, and (**c**) Mangart.

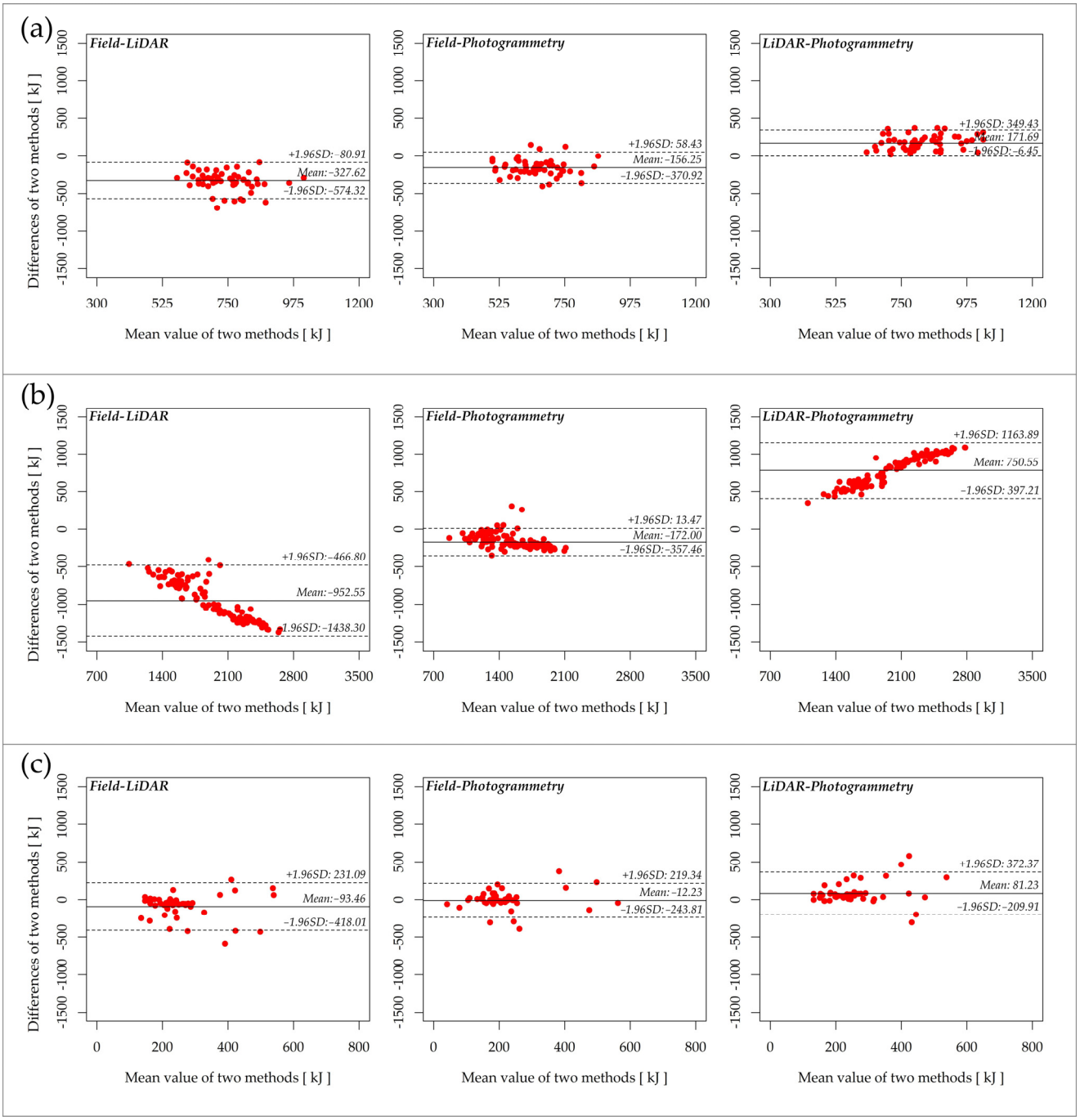


**Figure 15.** Bland–Altman plot for the differences in maximum kinetic energies (E_95CI) between any combination of rock measurement methods (field measurement, LiDAR point cloud, and photogrammetric point cloud) for (**a**) Kekec, (**b**) Krnica, and (**c**) Mangart.

**Table 9.** Statistical distribution of maximum passing heights (m) for methods based on field measurements and measurements based on LiDAR and photogrammetric point cloud methods.

| Method | MIN | Q1 | Median | Q3 | MAX |
|---|---|---|---|---|---|
| **Kekec Site** | | | | | |
| Field | 1.72 | 1.72 | 1.72 | 1.74 | 1.99 |
| LiDAR | 1.95 | 1.95 | 1.95 | 1.96 | 2.22 |
| Photogrammetry | 1.88 | 1.88 | 1.88 | 1.88 | 2.15 |
| **Krnica Site** | | | | | |
| Field | 2.03 | 2.14 | 2.20 | 2.41 | 4.45 |
| LiDAR | 2.32 | 2.47 | 2.56 | 2.71 | 4.57 |
| Photogrammetry | 2.10 | 2.22 | 2.30 | 2.52 | 4.50 |
| **Mangart Site** | | | | | |
| Field | 1.13 | 1.24 | 1.33 | 2.10 | 4.36 |
| LiDAR | 1.20 | 1.29 | 1.42 | 2.25 | 4.17 |
| Photogrammetry | 1.13 | 1.23 | 1.36 | 1.69 | 4.59 |

The Passing–Bablok regression analysis (Figure 16) shows a good agreement with all pairs of measuring methods at all sites, with intercept values that are close to 0 (<1) and slope values that are close to 1. Pearson's correlation coefficient (r) showed that these methods were highly correlated in the case of the Kekec and Krnica sites ($r > 0.889$), while the correlation was lower at the Mangart site since individual values express larger differences.

However, the Bland–Altman plot reveals that the mean differences at the Mangart site are close to 0 with respect to all methods (Figure 17). Similar conclusions can be obtained for the two other sites.

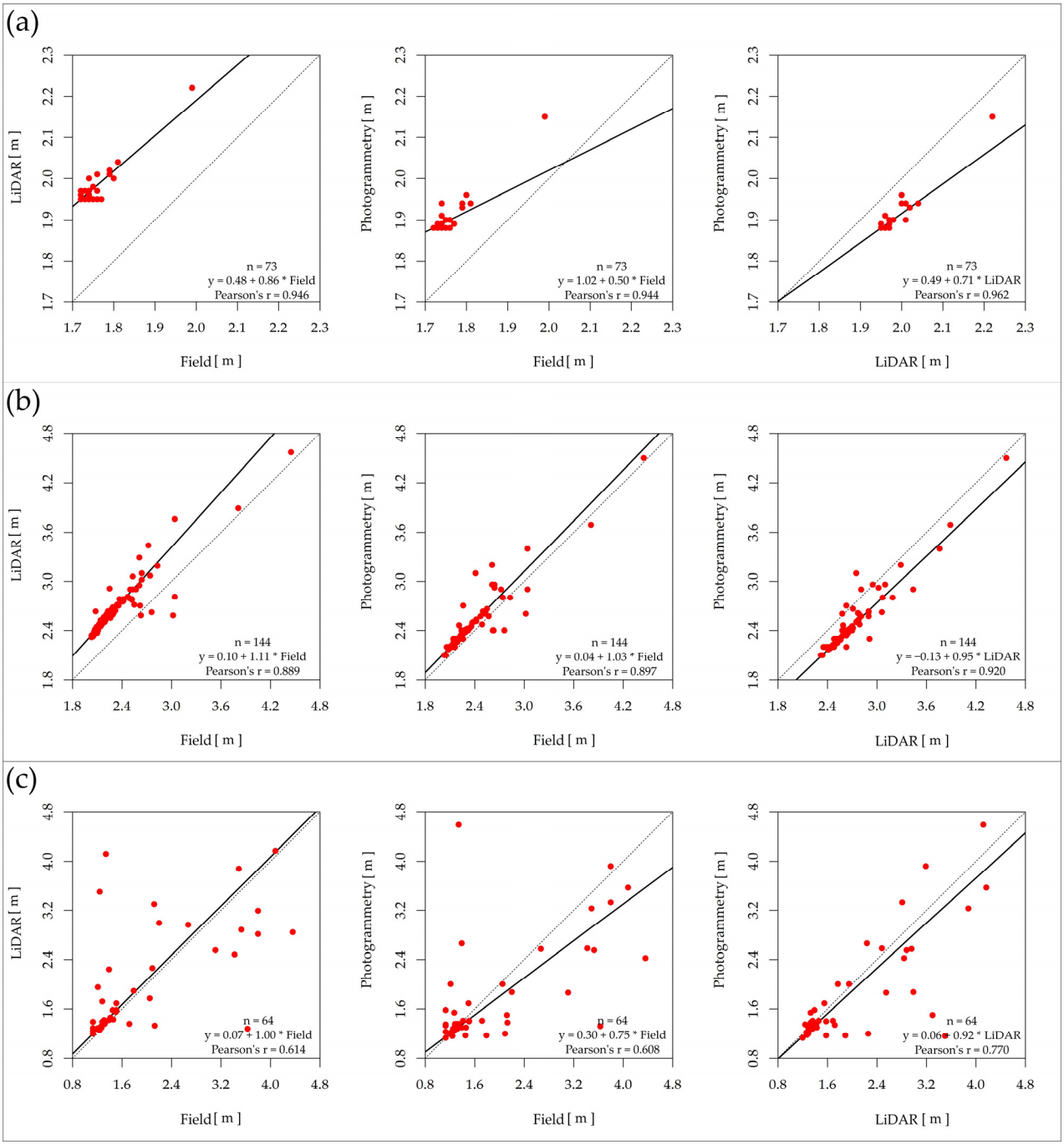


**Figure 16.** Passing–Bablok regression analysis for maximum passing heights (Ph_95CI) for different pairs of measuring methods (field measurement, LiDAR point cloud, and photogrammetric point cloud) for (**a**) Kekec, (**b**) Krnica, and (**c**) Mangart.

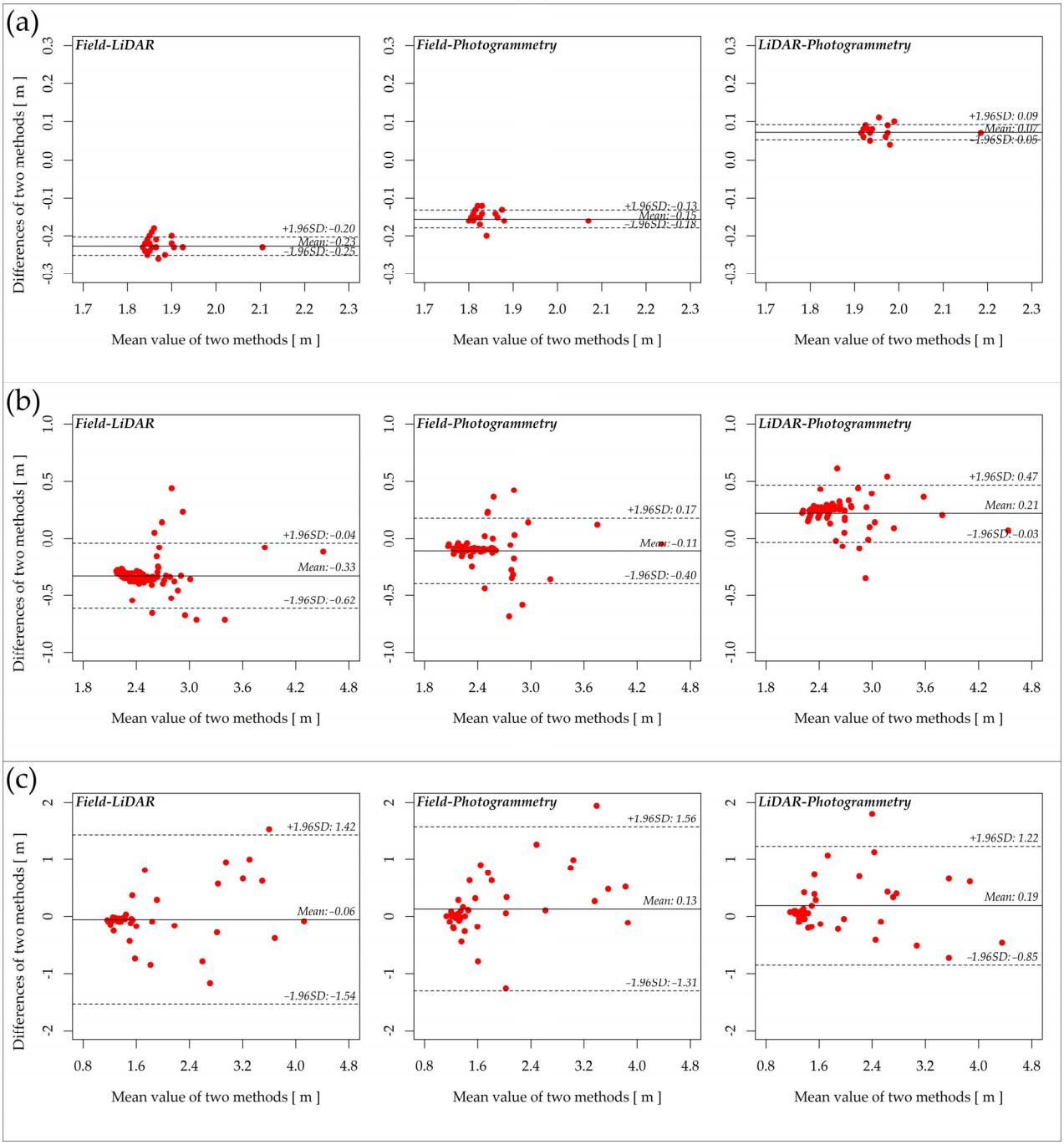


**Figure 17.** Bland–Altman plot for differences in the maximum passing heights (Ph_95CI) between any combination of rock measurement methods (field measurement, LiDAR point cloud, and photogrammetric point cloud) for (**a**) Kekec, (**b**) Krnica, and (**c**) Mangart.

## 4. Discussion

Different UAV remote sensing techniques have an important role in reconstructing past rockfall activity and in modeling potential rockfall runout zones in order to reduce rockfall risks posed to human activities. They can significantly reduce the number of conventional field surveys and further improve the safety of field operations [75]. The main aim of the study was to reconstruct the dimensions of a 3D rock object from a point cloud that is either based on photogrammetry or LiDAR scanning and to use them as input parameters in a rockfall model that simulated the trajectories and runout areas of rockfalls. A comparative analysis of measurements from point clouds was also performed for the

modeling results of classical measurement approaches when rocks are measured in the field. The motivation behind this study is to obtain improved safety conditions and to reduce the time needed for performing surveys in rockfall-exposed areas.

Several complex methods for extracting rock dimensions from point clouds are available [35–37,63]. Those methods include several factors for defining rocks that can be detached from the rock walls (e.g., joints and plane intersect) since the height of the rocks cannot be easily determined. Consequently, there is a need for using more complex algorithms that are time-consuming during extraction processes. In our study, an envelope method based on the minimum bounding volume was used for extracting the dimensions (width, length, and height) of rock deposits in the runout areas. The method has proven to be successful, and as the majority of deposits rocks can be observed from all directions (if they are not buried by other rocks), the extraction of dimensions can be performed by using less complex algorithms that are also less computationally intensive and could potentially be used by different users with different expertise knowledge relative to processing point clouds. However, when using a minimum bounding volume method, it must be taken into account that the method can largely be sensitive to potential outliers [63]; thus, it is critical that the extraction of individual rocks from points clouds is carried out precisely.

The comparison of dimensions and volumes, extracted from photogrammetric and LiDAR point cloud methods, has shown that the differences in the results of the field measurements are not statistically significant. Moreover, the differences are also negligible in the case of modeling rockfall propagation areas, meaning that the inputs of measurements based on all three methods can successfully be used in modeling rockfall runout zones. Generally, the values differ within a similar range with respect to all three methods; the noticeable differences are only that the measurements of LiDAR point clouds on average achieved the largest values, while field measurements achieved the lowest values. Statistically significant differences between the measurement methods were present when comparing the modeled maximum kinetic energies; here, measurements from LiDAR scanning methods achieved values that were larger by more than one degree compared to field and photogrammetric measurements. Since the inputted dimensions of the rocks in the model are the largest when using LiDAR measurements, the expected kinetic energies will consequently be larger due to the mass of the rock. Additionally, the rocks will have a slightly different interaction with the ground and produce different traveling trajectories compared to using field and photogrammetry methods, and rocks will be deposited higher up-slope than in the case of LiDAR measurements. On the other hand, the differences between the maximum passing heights are almost negligible; this shows that the model is less sensitive to the changes in the inputted rock dimension parameters and passing heights, which are more related to the surface's roughness and are constant in the case of all methods. The largest differences in the passing heights would be expected in areas that are in contact with the forest. However, based on the used methodology of extracting both kinetic energy and passing height values, none of the rocks within high or medium hazard risk are not located in the forest, while also no rocks were located within the calculated low hazard risk that is located within the forest at two study sites. The values of the maximum passing height at the Mangart site were more scattered when comparing field measurements to LiDAR or photogrammetric measurements at the other two locations. The Mangart runout zone is less homogeneous (meadow with rockfall deposits and surface rockiness) than in the case of Kekec/Krnica (terrain with scree materials), and this homogeneity is expressed in modeling results. The trajectories between the measuring methods are not identical due to different inputted rock dimensions, meaning that interactions with the ground (in the model represented with DTM) will not be the same. Since meadow terrain is mixed with rocks at the Mangart site, traveling rocks have different trajectories in the model and they can be more or less in contact with the ground (grass), or other rocks can be present on the ground. This is reflected in the variety of maximum passing heights as the rebound is related to the type of ground surface. The surface roughness values between rg70, rg20, and rg10 have smaller differences in the case of the Kekec and Krnica

sites than with the Mangart site, which is based on the mean obstacle size of the ground. Larger differences express larger possible deviations with respect to how rocks rebound in the model. However, the mean values are still comparable between the methods.

Commonly, field measurements are called and used as "truthful data" in different rockfall modeling analyses [8,14,20,21]. However, in our experience and based on the results of this study, we argue that the field measurements of rock dimensions might not always represent the best results. Measuring rocks on steep slopes presents a challenge itself, in addition to the surface's roughness. Moreover, when in the field, we were not able to estimate the geometry of the individual rock; in these cases, we would measure the largest width, length, or height extent. Even though we can help by identifying simple rock shapes—e.g., rectangular, ellipsoidal, spherical, and disc shapes [11]—defining the location of maximum extents is impossible. This will be even more difficult with larger rocks that have irregular shapes; with those, we cannot clearly determine the contact of the rocks with ground/other rocks when measuring the height. From this perspective, the measurements of a rock's dimensions might not be consistent and can consequently result in unrepresentative measurements [63]. This is reflected also in our results where the rock field measurements were underestimated compared to measurements using photogrammetric and LiDAR point cloud methods at all study sites. The following two methods have largely comparable results, with LiDAR measurement results being slightly more representative of the rockfall propagation probability modeling results. The measurement of rock dimensions with the proposed minimum bounding volume method can be compared to field measurements and provide more harmonized data that are associated with less bias-related tape measurements, which require recording the measured values by hand (and are related to possible human mistakes). Moreover, the method can decrease the time needed for preparing input data and parameters for rockfall runout modeling. Since surface roughness parameters are related to rock heights, both parameters can be extracted from point clouds using the proposed methodology.

Nevertheless, measurements from both LiDAR and photogrammetric point cloud methods can successfully be used as sources of input parameters for rockfall modeling. The differences between methods can be exhibited in situations where there are vegetated areas (e.g., forests, bushes, and tall grass). In those cases, the LiDAR point cloud method is more advantageous due to the penetrating ability of laser pulses that can be propagated through vegetation. Moreover, LiDAR scanning is less affected by lightning conditions than photogrammetric surveys. Photogrammetry relies more on the reflections of light from the imaged surface or object; therefore, factors such as cloud cover, camera angle, the time of the day, etc., can greatly affect final products. The overlap between images must be high enough to achieve the desired accuracy of the data (e.g., point density), while it is possible to cover larger areas to achieve the same result with LiDAR [76]. LiDAR pulses can also exhibit deeper penetration, and they can obtain more points on the sides of the rocks, resulting in a higher-density point cloud, which further enables more precise estimations of the shape of the rock and its dimensions. The following can be particularly crucial for measuring the height of rocks. The identification of rocks in LiDAR point clouds is strictly bound to the geometry of the surface; thus, interpreting the data can be more difficult. In colorized point clouds, the distinction between the rock and, e.g., neighboring rocks or vegetation (e.g., bush or tall grass) can be clearer [38].

Using an envelope of the minimum bounding volume is a relatively simplified method of reconstructing rock dimensions, and it is not demanding from a computational point of view [63]. A method such as this one could enable the collection of larger samples of rock deposits in comparison to the number of rocks that could potentially be measured on the field in, e.g., one day. Larger samples would therefore mean a more truthful representation of the actual rock dimensions and volumes. The increased samples of rock deposits, which can be obtained with this methodology, can then assist in the validation of rockfall models both on local and, especially, regional scales, potentially enabling the increased

identification of rockfall risks at larger scales and resulting in the improved planning of rockfall protection measures and the management of rockfall protective forests [60,77,78].

From the perspective of modeling the rockfall runout area, all three measuring methods have proven to be successful and equal since the small differences in the rock dimensions do not provide significantly different modeled propagation areas. On the other hand, within the modeled propagation area, the largest differences due to changed input values with respect to rock dimensions were observed in the maximum kinetic energies but not for maximum passing heights. Consequently, when planning technical protection (e.g., nets), the source of the rock measurement will be crucial, especially since the measurements on the field can provide "false negative" results by not detecting higher kinetic energies, and rockfall risks with the protection measures cannot be significantly minimized to provide safety for human activities. Based upon these observations, measurements from LiDAR point clouds prove to be more effective solutions, with results that provide improved safety from the aspect of predicting maximum kinetic energies. Moreover, different approaches should be tested with respect to how maximum kinetic energy and passing height values are extracted—such as by not extracting them at the local scale and by considering the location of individual rock deposits within the entire rockfall propagation area.

## 5. Conclusions

This study has shown the application of UAV-acquired LiDAR and photogrammetric point clouds for measuring rock dimensions in order to provide input parameters for modeling rockfall propagation areas. The purpose of the study was to show that these datasets can be used as an alternative to the traditional approach of measuring rock dimensions on the field by using a measuring tape. With UAV surveys, it is possible to cover larger areas and obtain data at larger scales, with decreased fieldwork efforts and most importantly improved safety conditions for fieldwork at rockfall areas. This study provided a comparison of measurement methods with respect to rock dimensions (width, length, and height) between field, LiDAR, and photogrammetric survey methods.

The results of this study show that the minimum bounding volume method can be used for extracting the dimensions of rocks from LiDAR and photogrammetric point clouds since the measured values are comparable to those on the field. The differences between all methods were also not statistically significant when comparing the volumes of the rocks. LiDAR measurements provide the largest mean values with respect to dimensions and volume, while field measurements provided the lowest values. Nevertheless, when using the mean dimension values as inputs into the model, the GOF indexes have shown that the model has similar rockfall propagation probability prediction rates in the case of all three methods. LiDAR-derived dimensions provide slightly better results.

From the rockfall modeling results, maximum kinetic energies and maximum passing heights were compared between the three measuring methods. Even though there were no statistically significant differences between the maximum passing heights, they were present for the maximum kinetic energies. The following modeling output resulted in values that were more than one-time larger compared to the measurements obtained using photogrammetric point clouds and field measurements. Based on the results of the study, we can conclude that all three rock measurement methods can be used for defining the extent of rockfall propagation areas; in contrast, for planning technical protection measures, more in-depth considerations must be taken with respect to which measurement method will be used, particularly from the perspective that real kinetic energies cannot be missed and that protective measures are not planned sufficiently when attempting to reduce rockfall risks.

The study highlights the positive use of UAVs when providing input parameters for rockfall modeling, and it demonstrates how it is possible to overcome traditional and time-consuming surveys with the extraction of necessary rockfall parameters using either LiDAR or photogrammetric point cloud methods. Both point clouds can successfully be used in rockfall analyses, with LiDAR surveys being more appropriate in vegetated and

forested areas. However, based on the higher cost that LiDAR sensors present compared to camera sensors, photogrammetry can also be a good alternative, as was proven by the results of this study.

**Author Contributions:** Conceptualization, B.Ž., F.B. and M.K.; methodology, B.Ž., F.B. and M.K.; formal analysis, B.Ž.; investigation, B.Ž.; resources, F.B. and M.K.; data curation, B.Ž., F.B. and M.K.; writing—original draft preparation, B.Ž.; writing—review and editing, F.B. and M.K.; visualization, B.Ž. and M.K.; supervision, F.B. and M.K. All authors have read and agreed to the published version of the manuscript.

**Funding:** The authors express their gratitude to the Pahernik Foundation for providing funds to prepare this paper. This research was also supported by the Slovenian Research Agency project J1-3024 (Deciphering the sensitivity of rock faces to climatic changes and freeze-thaw cycles in permafrost-free regions) and Interreg Alpine Space projects "ROCKtheALPS" (ASP 462) and "GreenRisk4ALPs" (ASP 635). The third author acknowledges the financial support from the Slovenian Research Agency (research core funding No. P4-0059).

**Data Availability Statement:** The data presented in this study are available upon request from the corresponding author.

**Acknowledgments:** The first author additionally thanks the Pahernik Foundation for co-financing the tuition for the doctoral study, of which this paper presents one of the major results. Special thanks also goes to the Triglav National Park for issuing a permit for conducting research within the park.

**Conflicts of Interest:** The authors declare no conflict of interest.

## References

1. D'Amato, J.; Hantz, D.; Guerin, A.; Jaboyedoff, M.; Baillet, L.; Mariscal, A. Influence of meteorological factors on rockfall occurrence in a middle mountain limestone cliff. *Nat. Hazards Earth Syst. Sci.* **2016**, *16*, 719–735. [CrossRef]
2. Lopez-Saez, J.; Corona, C.; Eckert, N.; Stoffel, M.; Bourrier, F.; Berger, F. Impacts of land-use and land-cover changes on rockfall propagation: Insights from the Grenoble conurbation. *Sci. Total Environ.* **2016**, *547*, 345–355. [CrossRef] [PubMed]
3. Corominas, J.; Mavrouli, O.; Ruiz-Carulla, R. Rockfall Occurrence and Fragmentation. In *Advancing Culture of Living with Landslides*; Sassa, K., Mikoš, M., Yin, Y., Eds.; WLF 2017; Springer: Cham, Switzerland, 2017. [CrossRef]
4. Giordan, D.; Cignetti, M.; Godone, D.; Bertolo, D.; Paganone, M. Definition of an operative methodology for the management of Rockfalls along with the Road Network. *Sustainability* **2021**, *13*, 7669. [CrossRef]
5. Crosta, G.B.; Agliardi, F.; Frattini, P.; Lari, S. Key Issues in Rock Fall Modeling, Hazard and Risk Assessment for Rockfall Protection. In *Engineering Geology for Society and Territory—Volume 2*; Springer: Cham, Switzerland, 2015. [CrossRef]
6. Cruden, D.M.; Varnes, D.J. Landslide Types and Processes, Special Report, Transportation Research Board. *Natl. Acad. Sci.* **1996**, *247*, 36–75.
7. Vanneschi, C.; Camillo, M.D.; Aiello, E.; Bonciani, F.; Salvini, R. SFM-MVS photogrammetry for rockfall analysis and hazard assessment along the ancient roman via Flaminia road at the Furlo gorge (Italy). *ISPRS Int. J. Geo-Inf.* **2019**, *8*, 325. [CrossRef]
8. Ruiz-Carulla, R.; Corominas, J. Analysis of Rockfalls by Means of a Fractal Fragmentation Model. *Rock Mech. Rock Eng.* **2020**, *53*, 1433–1455. [CrossRef]
9. Dorren, L.; Berger, F.; Bourrier, F.; Eckert, N.; Saroglou, C.; Schwarz, M.; Stoffel, M.; Trappmann, D.; Utelli, H.-H.; Moos, C. Delimiting rockfall runout zones using reach probability values simulated with a Monte-Carlo based 3D trajectory model. *Nat. Hazards Earth Syst. Sci. Discuss.* **2022**, 1–23, *preprint*.
10. Volkwein, A.; Schellenberg, K.; Labiouse, V.; Agliardi, F.; Berger, F.; Bourrier, F.; Dorren, L.K.A.; Gerber, W.; Jaboyedoff, M. Rockfall characterisation and structural protection—A review. *Nat. Hazards Earth Syst. Sci.* **2011**, *11*, 2617–2651. [CrossRef]
11. Dorren, L.K.A. Rockyfor3D (v5.2) Revealed. In *Transparent Description of the Complete 3D Rockfall Model*; International Association for Natural Hazard Risk Management EcorisQ: Geneva, Switzerland, 2016; p. 32.
12. Yan, P.; Zhang, J.; Kong, X.; Fang, Q. Numerical simulation of rockfall trajectory with consideration of arbitrary shapes of falling rocks and terrain. *Comput. Geotech.* **2020**, *122*, 103511. [CrossRef]
13. Jaboyedoff, M.; Dudt, J.P.; Labiouse, V. An attempt to refine rockfall hazard zoning based on the kinetic energy, frequency and fragmentation degree. *Nat. Hazards Earth Syst. Sci.* **2005**, *5*, 621–632. [CrossRef]
14. Žabota, B.; Kobal, M. A new methodology for mapping past rockfall events: From mobile crowdsourcing to rockfall simulation validation. *ISPRS Int. J. Geo-Inf.* **2020**, *9*, 514. [CrossRef]
15. Dussauge, C.; Helmstetter, A.; Grasso, J.; Hantz, S.; Desvarreux, P.; Jeannin, M.; Giraud, A. Probabilistic approach to rockfall hazard assessment: Potential of historical data analysis. *Nat. Hazards Earth Syst. Sci.* **2002**, *2*, 15–26. [CrossRef]
16. Dussauge, C.; Grasso, J.; Helmstetter, A. Statistical Analysis of Rock Fall Volume Distributions: Implications for Rock fall Dynamics. *J. Geophys. Res.* **2003**, *108*, 2286.

17. Lari, S.; Frattini, P.; Crosta, G.B. A probalistic approach for landslide hazard analysis. *Eng. Geol.* **2014**, *182*, 3–14. [CrossRef]
18. De Biagi, V.; Lia Napoli, M.; Barbero, M.; Peila, D. Estimation of the return period of rockfalls according to the block size. *Nat. Hazards Earth Syst. Sci.* **2016**, *17*, 103–113. [CrossRef]
19. Haas, F.; Heckmann, T.; Wichmann, V.; Becht, M. Runout analysis of a large rockfall in the Dolomites/Italian Alps using LIDAR derived particle sizes and shapes. *Earth Surf. Process. Landf.* **2012**, *37*, 1444–1455. [CrossRef]
20. Macciotta, R.; Gräpel, C.; Skirrow, R. Fragmented rockfall volume distribution from photogrammetry-based structural mapping and discrete fracture networks. *Appl. Sci.* **2020**, *10*, 6977. [CrossRef]
21. Ruiz-Carulla, R.; Corominas, J.; Mavrouli, O. A Methodology to Obtain the Block Size Distribution of Fragmental Rockfall Deposits. *Landslides* **2015**, *12*, 815–825. [CrossRef]
22. Marchelli, M.; De Biagi, V. Optimization methods for the evaluation of the parameters of a rockfall fractal fragmentation model. *Landslides* **2019**, *16*, 1385–1396. [CrossRef]
23. Wegner, K.; Haas, F.; Heckmann, T.; Mangeney, A.; Durand, V.; Villeneuve, N.; Kowalski, P.; Peltier, A.; Becht, M. Assessing the effect of lithological setting, block characteristic and slope topography on the runout length of rockfalls in the Alps and on the La Réunion island. *Nat. Hazards Earth Syst. Sci.* **2020**, 1–27. [CrossRef]
24. Albarelli, D.S.N.A.; Mavrouli, O.C.; Nyktas, P. Identification of potential rockfall sources using UAV-derived point cloud. *Bull. Eng. Geol. Environ.* **2021**, *80*, 6539–6561. [CrossRef]
25. Žabota, B.; Kobal, M. Accuracy Assessment of UAV-Photogrammetric-Derived Products Using PPK and GCPs in Challenging Terrains: In Search of Optimized Rockfall Mapping. *Remote Sens.* **2021**, *13*, 3812. [CrossRef]
26. Kenner, R.; Gischig, V.; Gojcic, Z.; Quéau, Y.; Kienholz, C.; Figi, D.; Thöny, R.; Bonanomi, Y. The potential of point clouds for the analysis of rock kinematics in large slope instabilities: Examples from the Swiss Alps: Brinzauls, Pizzo Cengalo and Spitze Stei. *Landslides* **2022**, *19*, 1357–1377. [CrossRef]
27. Sarro, R.; Riquelme, A.; García-Davalillo, J.; Mateos, R.; Tomás, R.; Pastor, J.; Cano, M.; Herrera, G. Rockfall Simulation Based on UAV Photogrammetry Data Obtained during an Emergency Declaration: Application at a Cultural Heritage Site. *Remote Sens.* **2018**, *10*, 1923. [CrossRef]
28. Danzi, M.; Di Crescenzo, G.; Ramondini, M.; Santo, A. Use of unmanned aerial vehicles (UAVs) for photogrammetric surveys inrockfall instability studies. *Rend. Online Soc. Geol. Ital.* **2013**, *24*, 82–85.
29. Žabota, B.; Kobal, M. The Use of UAV-Acquired Multiband Images for Detecting Rockfall-Induced Injuries at Tree Crown Level. *Forests* **2022**, *13*, 1039. [CrossRef]
30. Salvini, R.; Mastrorocco, G.; Esposito, G.; Di Bartolo, S.; Coggan, J.; Vanneschi, C. Use of a remotely piloted aircraft system for hazard assessment in a rocky mining area (Lucca, Italy). *Nat. Hazards Earth Syst. Sci.* **2018**, *18*, 287–302. [CrossRef]
31. Kim, D.H.; Gratchev, I.; Berends, J.; Balasubramaniam, A. Calibration of restitution coefficients using rockfall simulations based on 3D photogrammetry model: A case study. *Nat. Hazards* **2015**, *78*, 1931–1946. [CrossRef]
32. Lato, M.J.; Hutchinson, D.J.; Gauthier, D.; Edwards, T.; Ondercin, M. Comparison of airborne laser scanning, terrestrial laser scanning, and terrestrial photogrammetry for mapping differential slope change in mountainous terrain. *Can. Geotech. J.* **2015**, *52*, 129–140. [CrossRef]
33. Santangelo, M.; Alvioli, M.; Baldo, M.; Cardinali, M.; Giordian, D.; Guzzetti, F.; Marchesini, I.; Reichenbach, P. Brief communication: Remotely piloted aircraft systems for rapid emergency response: Road exposure to rockfall in Villanova di Accumoli. *Nat. Hazards Earth Syst. Sci.* **2019**, *19*, 325–335. [CrossRef]
34. Konstantinidis, I.; Marinos, V.; Papathanassiou, G. UAV-based evaluation of rockfall hazard in the cultural heritage area of kipinas monastery, Greece. *Appl. Sci.* **2021**, *11*, 8946. [CrossRef]
35. Chen, N.; Kemeny, J.; Jiang, Q.; Pan, Z. Automatic extraction of blocks from 3D point clouds of fractured rock. *Comput. Geosci.* **2017**, *109*, 149–161. [CrossRef]
36. Wichmann, V.; Strauhal, T.; Fey, C.; Perzlmaier, S. Derivation of space-resolved normal joint spacing and in situ block size distribution data from terrestrial LIDAR point clouds in a rugged Alpine relief (Kühtai, Austria). *Bull. Eng. Geol. Environ.* **2019**, *78*, 4465e4478. [CrossRef]
37. Mavrouli, O.; Corominas, J.; Jaboyedoff, M. Size distribution for potentially unstable rock masses and in situ rock blocks using LIDAR-generated digital elevation models. *Rock Mech. Rock Eng.* **2015**, *48*, 1589e1604. [CrossRef]
38. Spreafico, M.C.; Franci, F.; Bitelli, G.; Borgatti, L.; Ghirotti, M. Intact rock bridge breakage and rock mass fragmentation upon failure: Quantification using remote sensing techniques. *Photogramm. Rec.* **2017**, *32*, 513–536. [CrossRef]
39. Robiati, C.; Eyre, M.; Vanneschi, C.; Francioni, M.; Venn, A.; Coggan, J. Application of remote sensing data for evaluation of rockfall potential within a quarry slope. *ISPRS Int. J. Geo-Inf.* **2019**, *8*, 367. [CrossRef]
40. Francioni, M.; Antonaci, F.; Sciarra, N.; Robiati, C.; Coggan, J.; Stead, D.; Calamita, F. Application of Unmanned Aerial Vehicle Data and Discrete Fracture Network Models for Improved Rockfall Simulations. *Remote Sens.* **2020**, *12*, 2053. [CrossRef]
41. Gallo, I.G.; Martínez-Corbella, M.; Sarro, R.; Iovine, G.; López-Vinielles, J.; Hérnandez, M.; Robustelli, G.; Mateos, R.M.; García-Davalillo, J.C. An Integration of UAV-Based Photogrammetry and 3D Modelling for Rockfall Hazard Assessment: The Cárcavos Case in 2018 (Spain). *Remote Sens.* **2021**, *13*, 3450. [CrossRef]
42. Placer, L. Osnovne tektonske razčlenitve Slovenije. *Geologija* **2008**, *51*, 205–217. [CrossRef]
43. Jurkovšek, B. *Tolmač Listov Beljak in Ponteba: Osnovna Geološka Karta, SFRJ 1:100,000*; Zvezni Geološki Zavod: Belgrade, Serbia, 1987; p. 55.

44. Jurkovšek, B.; Šribar, L.; Ogorelec, B.; Kolar-Jurkovšek, T. Pelagic Jurassic and Cretaceous beds in the western part of the Julian Alps. *Geologija* **2020**, *31*, 285–328.
45. MAVIC 2. Available online: https://www.dji.com/si/mavic-2 (accessed on 9 November 2022).
46. MATRICE 600. Available online: https://www.dji.com/si/matrice600 (accessed on 9 November 2022).
47. YellowScan Surveyor Ultra. Available online: https://www.yellowscan-lidar.com/products/surveyor-ultra/ (accessed on 9 November 2022).
48. Ground Station Software. Available online: https://www.ugcs.com/ (accessed on 9 November 2022).
49. SMARS. *LiDAR Data in D96TM Projection*; The Surveying and Mapping Authority of the Republic Slovenia: Ljubljana, Slovenia, 2014.
50. Kyriou, A.; Nikolakopoulos, K.; Koukouvelas, I. How image acquisition geometry of UAV campaigns affects the derived products and their accuracy in areas with complex geometry. *ISPRS Int. J. Geo.-Inf.* **2021**, *10*, 408. [CrossRef]
51. Pix4Dmapper—Pix4D. Available online: https://www.pix4d.com/product/pix4dmapper-photogrammetry-software (accessed on 11 November 2022).
52. POSPac UAV. Available online: https://www.applanix.com/products/pospac-uav.htm (accessed on 11 November 2022).
53. YellowScan CloudStation. Available online: https://www.yellowscan-lidar.com/products/cloudstation/ (accessed on 11 November 2022).
54. TerraMatch. Available online: https://terrasolid.com/products/terramatch/ (accessed on 11 November 2022).
55. Heim, A. *Bergsturz und Menschenleben*; No. 20; Fretz & Wasmuth: Tübingen, Germany, 1932.
56. Toe, D.; Berger, F. Regional Mapping of Forest with a Protection Function Against Rockfall. In *Engineering Geology for Society and Territory*; Lollino, G., Giordan, D., Crosta, G.B., Corominas, J., Azzam, R., Wasowski, J., Sciarra, N., Eds.; Springer International Publishing: Cham, Switzerland, 2015; Volume 2, pp. 1957–1959.
57. Berger, F.; Dorren, L.K.A. Principles of the tool Rockfor.net for quantifying the rockfall hazard below a protection forest. *Schweiz. Z. Forstwes.* **2007**, *158*, 157–165. [CrossRef]
58. MEZAP. *Note Méthodologique « MEZAP » Caractérisation de l'aléa Rocheux dans le Cadre d'un Plan de Prévention des Risques Naturels (PPRn) ou d'un Porter à Connaissance (PAC). Rédaction et Validation par le Groupe de travail MEZAP (BRGM, CEREMA, DDTM 06, DDT 38, DDT 73, DDT74, INERIS, INRAE, MTE/DGPR, ONF-RTM, Univ. G. Eiffel)*; Guide technique: Aléa rocheux; Colas, B., Berger, F., Martin, R., Eds.; Frédéric Simien (head of BRGM Éditions) and Amanda Hoffbourg; Agence Chromatiques: Paris, France, 2015; 68p.
59. Dupire, S.; Toe, D.; Barré, J.B.; Bourrier, F.; Berger, F. Harmonized mapping of forests with a protection function against rockfalls over European Alpine countries. *Appl. Geogr.* **2020**, *120*, 102221. [CrossRef]
60. Levy, C.; Colas, B.; Rohmer, J.; Berger, F. ELANA (Energy Line Angle Normalized Area): Un outil d'aide à la cartographie de la propagation des chutes de blocs basée sur la méthode de la ligne d'énergie à différentes échelles. In Proceedings of the 5th RSS Rock Slope Stability Symposium, Chambéry, France, 16–18 November 2021; pp. 1–2.
61. CloudCompare. Available online: https://www.danielgm.net/cc/ (accessed on 9 November 2022).
62. ArcGIS Pro 2.7.3, Esri. Available online: https://www.esri.com/en-us/arcgis/products/arcgis-pro/resources (accessed on 9 November 2022).
63. Bonneau, D.A.; Jean Hutchinson, D.; DiFrancesco, P.M.; Coombs, M.; Sala, Z. Three-dimensional rockfall shape back analysis: Methods and implications. *Nat. Hazards Earth Syst. Sci.* **2019**, *19*, 2745–2765. [CrossRef]
64. Feldens, P.; Darr, A.; Feldens, A.; Tauber, F. Detection of Boulders in Side Scan Sonar Mosaics by a Neural Network. *Geosciences* **2019**, *9*, 159. [CrossRef]
65. Dorren, L.K.A.; Heuvelink, G.B.N. Effect of support size on the accuracy of a distributed rockfall model. *Int. J. Geog. Inf. Sci.* **2004**, *18*, 595–609. [CrossRef]
66. Žabota, B.; Mikoš, M.; Kobal, M. Rockfall modelling in forested areas: The role of digital terrain model grid cell size. *Appl. Sci.* **2021**, *11*, 1461. [CrossRef]
67. Corona, C.; Lopez-Saez, J.; Favillier, A.; Mainieri, R.; Eckert, N.; Trappmann, D.; Stoffel, M.; Bourrier, F.; Berger, F. Modeling rockfall frequency and bounce height from three-dimensional simulation process models and growth disturbances in submontane broadleaved trees. *Geomorphology* **2017**, *281*, 66–77. [CrossRef]
68. Slovenian Forest Service. Forest Stand Data. Available online: http://prostor.zgs.gov.si/pregledovalnik/?locale=en (accessed on 9 November 2020).
69. RStudio Team. *RStudio: Integrated Development for R*; RStudio Inc.: Boston, MA, USA, 2016.
70. McArdle, B.H.; Anderson, M.J. Fitting multivariate models to community data: A comment on distance-based redundancy analysis. *Ecology* **2001**, *82*, 290–297. [CrossRef]
71. Passing, H.; Bablok, W. A new biometrical procedure for testing the equality of measurements from two different analytical methods. Application of linear regression procedures for method comparison studies in Clinical Chemistry, Part I. *J. Clin. Chem. Clin. Biochem.* **1983**, *21*, 709–720. [CrossRef]
72. Bilić-Zulle, L. Comparison of methods: Passing and Bablok regression. *Biochem. Med.* **2011**, *21*, 49–52. [CrossRef] [PubMed]
73. Formetta, G.; Capparelli, G.; Versace, P. Evaluating performance of simplified physically based models for shallow landslide susceptibility. *Hydrol. Earth Syst. Sci.* **2016**, *20*, 4585–4603. [CrossRef]
74. Goodenough, D.J.; Rossmann, K.; Lusted, L.B. Radiographic applications of receiver operating characteristic (ROC) analysis. *Radiology* **1974**, *110*, 89–95. [CrossRef] [PubMed]

75. Loiotine, L.; Andriani, G.F.; Jaboyedoff, M.; Parise, M.; Derron, M.H. Comparison of remote sensing techniques for geostructural analysis and cliff monitoring in coastal areas of high tourist attraction: The case study of polignano a mare (southern Italy). *Remote Sens.* **2021**, *13*, 5045. [CrossRef]
76. Xu, Q.; Ye, Z.; Liu, Q.; Dong, X.; Li, W.; Fang, S.; Guo, C. 3D Rock Structure Digital Characterization Using Airborne LiDAR and Unmanned Aerial Vehicle Techniques for Stability Analysis of a Blocky Rock Mass Slope. *Remote Sens.* **2022**, *14*, 3044. [CrossRef]
77. Mateos, R.M.; García-Moreno, I.; Reichenbach, P.; Herrera, G.; Sarro, R.; Rius, J.; Aguiló, R.; Fiorucci, F. Calibration and validation of rockfall modelling at regional scale: Application along a roadway in Mallorca (Spain) and organization of its management. *Landslides* **2016**, *13*, 751–763. [CrossRef]
78. Cignetti, M.; Godone, D.; Bertolo, D.; Paganone, M.; Thuegaz, P.; Giordan, D. Rockfall susceptibility along the regional road network of Aosta Valley Region (northwestern Italy). *J. Maps* **2021**, *17*, 54–64. [CrossRef]